LETTER

Macromolecular organic compounds from the depths of Enceladus

Frank Postberg[1,2,3,13]*, Nozair Khawaja[1,13], Bernd Abel[4], Gael Choblet[5], Christopher R. Glein[6], Murthy S. Gudipati[7], Bryana L. Henderson[7], Hsiang-Wen Hsu[8], Sascha Kempf[8], Fabian Klenner[1], Georg Moragas-Klostermeyer[9], Brian Magee[6,8], Lenz Nölle[1], Mark Perry[10], René Reviol[1], Jürgen Schmidt[11], Ralf Srama[9], Ferdinand Stolz[4,12], Gabriel Tobie[5], Mario Trieloff[1,2] & J. Hunter Waite[6]

Saturn's moon Enceladus harbours a global water ocean[1], which lies under an ice crust and above a rocky core[2]. Through warm cracks in the crust[3] a cryo-volcanic plume ejects ice grains and vapour into space[4–7] that contain materials originating from the ocean[8,9]. Hydrothermal activity is suspected to occur deep inside the porous core[10–12], powered by tidal dissipation[13]. So far, only simple organic compounds with molecular masses mostly below 50 atomic mass units have been observed in plume material[6,14,15]. Here we report observations of emitted ice grains containing concentrated and complex macromolecular organic material with molecular masses above 200 atomic mass units. The data constrain the macromolecular structure of organics detected in the ice grains and suggest the presence of a thin organic-rich film on top of the oceanic water table, where organic nucleation cores generated by the bursting of bubbles allow the probing of Enceladus' organic inventory in enhanced concentrations.

Two mass spectrometers onboard the Cassini spacecraft, the Cosmic Dust Analyzer (CDA) and the Ion and Neutral Mass Spectrometer (INMS), performed compositional in situ measurements of material emerging from the subsurface of Enceladus. These measurements were made inside both the plume and Saturn's E ring, which is formed by ice grains escaping Enceladus' gravity[16].

The CDA records time-of-flight (TOF) mass spectra of cations generated by high-velocity impacts of individual grains onto a rhodium target, with a mass resolution of $m/\Delta m \approx 20$–50[14,17]. Previous CDA measurements showed that about 25% of the ice grain spectra of the E ring, the so-called type-2 spectra, exhibit the presence of organic material[8,9,14]. A subgroup (about 3%) of type-2 spectra (see Methods sections 'Dataset' and 'Relative frequency of HMOC-type grains depends on impact speed and distance to Enceladus orbit'; Extended Data Table 1) is characterized by a sequence of repetitive peaks beyond 80 u (where u is the unified atomic mass unit), usually separated by mass intervals of 12 u–13 u (Fig. 1). In most cases, this sequence extends to the maximum mass nominally covered by the CDA, about 200 u. The broad and irregular shape of the peaks indicates that they are composed of multiple unresolved overlapping mass lines (Fig. 1a and Extended Data Fig. 1). The mass intervals between the peaks suggest organic species with an increasing number of carbon atoms (C_7 to C_{15}), which we refer to as high-mass organic cations (HMOCs). While an interval of 14 u would indicate the addition of a saturated CH_2 group to an organic 'backbone', the actual average mass difference of 12.5 u indicates the presence of predominantly unsaturated carbon atoms.

In principle, each HMOC peak could be derived from a different parent molecule. However, a monotonic decrease without major intensity variations from 77 u to 191 u (Fig. 1a, Extended Data Fig. 1) rather indicate fragments from higher-mass parent molecules (outside the CDA's nominal mass range) and not a conglomerate of several molecules with masses below 200 u. This interpretation is consistent with the observation that the detection probability increases with impact speed (see Methods, 'Relative frequency of HMOC-type grains depends on impact speed and distance to Enceladus orbit'; Extended Data Table 1), increasing the available energy for fragmentation and ionization. A similar fragmentation pattern has been observed in impact experiments with polymers[18,19] containing aromatic subunits (Extended Data Fig. 2; see Methods, 'Inferring the origin of HMOC peaks in CDA spectra').

In addition to the nominal mass spectrum (1 u to ∼200 u), the CDA records extended TOF spectra of the same individual grains up to about 8,000 u with resolution and sensitivity uniformly reduced by a factor of ten. These extended spectra exhibit abundant macromolecular cations with masses in excess of 200 u in most HMOC-type spectra (Extended Data Fig. 5). This further supports the interpretation that fragmentation of macromolecular parent molecules or networks creates the HMOCs.

The HMOC sequence always appears together with intense non-water signatures below 80 u (Fig. 1), offering further compositional and structural constraints. Although there is some variation (Extended Data Figs. 1, 4), non-water peaks are arranged in six groups at 15 u, 27–31 u, 38–45 u, 51–58 u, 63–67 u, and 77–79 u and, like the HMOC pattern, indicate a sequence of organic species with increasing number of carbon atoms. Organic mass lines below 45 u appear preferentially at odd masses (Fig. 1b), indicating a typical cationic hydrocarbon fragmentation fingerprint. However, from stoichiometry, the mass lines at 30 u, 31 u, 44 u and 45 u cannot be pure hydrocarbon cations and indicate O- or N-bearing cations from hydroxyl (CH_2OH^+, CH_3–CH–OH^+), ethoxy or carbonyl functional groups or nitrogen-bearing ions (for example, $CH_2NH_2^+$ and CH_3–CH–NH_2^+) (Fig. 1b, Extended Data Fig. 4).

A prominent peak preceding the HMOC sequence (Fig. 1b) indicates abundant cationic forms of a benzene ring, phenyl ($C_6H_5^+$, 77 u) and benzenium ($C_6H_7^+$, 79 u). The high abundance of these cations is highly diagnostic because the energetically favourable cationic aromatic structure would be tropylium cations[18–20] ($C_7H_7^+$, 91 u) (Fig. 1a). Formation of tropylium cations must thus be inhibited, as it requires aromatic precursor molecules without hydrogenated C-atoms (for example, alkyl groups) attached to the ring[20,21] (see Fig. 2, Extended Data Fig. 7 and Methods section 'Inferring the origin of HMOC peaks in CDA spectra').

A high abundance of aromatic structures is further supported by mass lines at 63 u–65 u ($C_5H_{3,4,5}^+$), 51 u–53 u ($C_4H_{3,4,5}^+$) and 39 u (C_3H_3) (Fig. 1b, Extended Data Fig. 1), which can be interpreted as coincident unsaturated benzene fragments[21] (Fig. 2, Extended Data Fig. 7).

[1]Institut für Geowissenschaften, Universität Heidelberg, Heidelberg, Germany. [2]Klaus-Tschira-Labor für Kosmochemie, Universität Heidelberg, Heidelberg, Germany. [3]Institut für Geologische Wissenschaften, Freie Universität Berlin, Berlin, Germany. [4]Leibniz-Institute für Oberflächenmodifizierung (IOM), Leipzig, Germany. [5]Laboratoire de Planétologie et Géodynamique, UMR-CNRS 6112, Université de Nantes, Nantes, France. [6]Space Science and Engineering Division, Southwest Research Institute, San Antonio, TX, USA. [7]Jet Propulsion Laboratory, California Institute of Technology, Pasadena, CA, USA. [8]Laboratory for Atmospheric and Space Physics, University of Colorado, Boulder, CO, USA. [9]Institut für Raumfahrtsysteme, Universität Stuttgart, Stuttgart, Germany. [10]Applied Physics Laboratory, Johns Hopkins University, Laurel, MD, USA. [11]Astronomy Research Unit, University of Oulu, Oulu, Finland. [12]Wilhelm-Ostwald-Institut für Physikalische und Theoretische Chemie, Universität Leipzig, Leipzig, Germany. [13]These authors contributed equally: Frank Postberg, Nozair Khawaja. *e-mail: Frank.Postberg@geow.uni-heidelberg.de
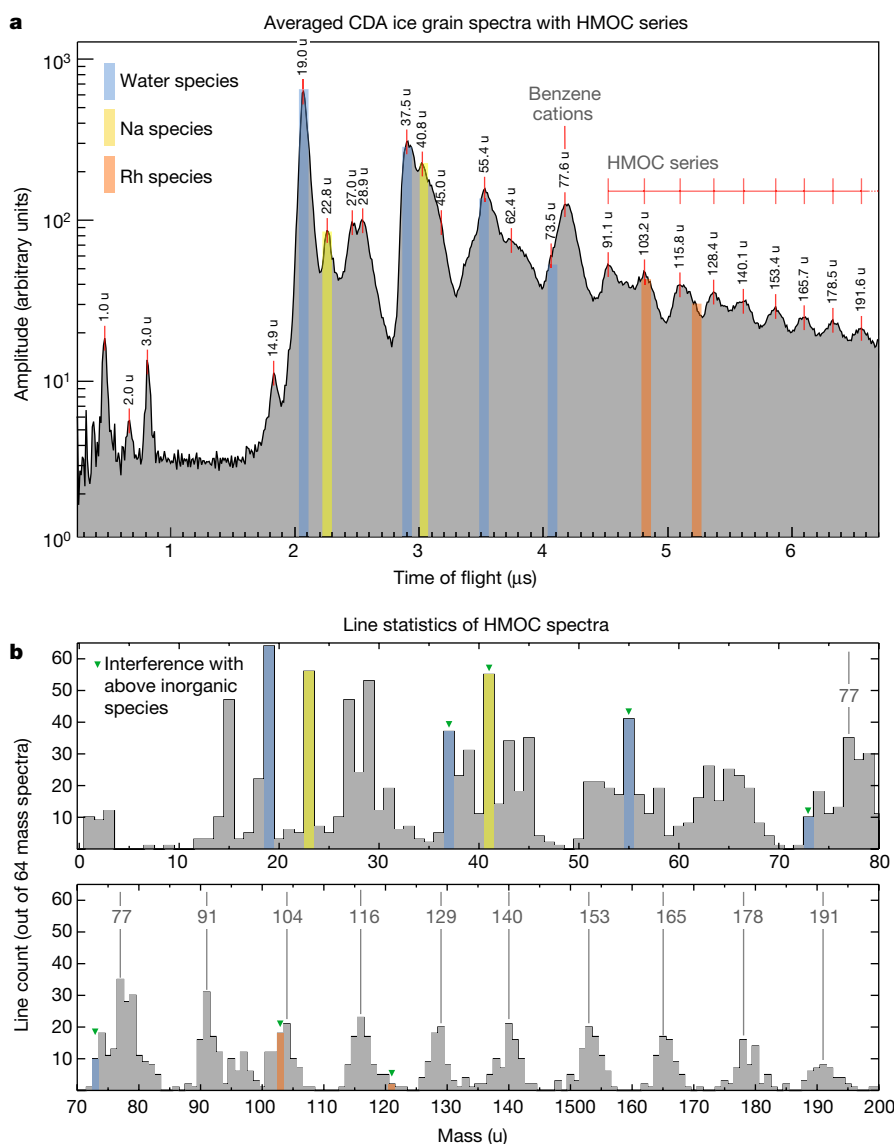
Fig. 1 | Co-added CDA HMOC spectrum and mass line histogram.
a, Time-of-flight spectrum representing the average of 64 high-quality spectra (see Methods, 'Selection of 64 high-quality spectra for Fig. 1 and Extended Data Figs. 1 and 3'). The amplitudes of individual spectra were normalized and co-added. The corresponding masses of the peaks are labelled. The spectrum provides a representation of the average abundance of cation species. All signatures that are not colour-shaded are exclusively or mostly due to organic cations, as described in the text. Mass lines of exclusively inorganic origin are H_3O^+ at 19 u and Na^+ at 23 u. Mass lines where interference with inorganic cations is likely are: $H_2O–H_3O^+$ (37 u), $H_2O–Na^+$ (41 u), $(H_2O)_2–H_3O^+$ (55 u) and $(H_2O)_3–H_3O^+$ (73 u). The CDA's target material, rhodium, and its water cluster forms cations at 103 u and 121 u (Rh^+, $Rh–H_2O^+$), respectively, that interfere with the HMOC pattern, but only in fast impacts (see Extended Data Fig. 3 for a comparison of fast versus slow impacts and Extended Data Fig. 4 for examples of individual CDA spectra; for a semi-quantitative overview of spectral features in individual spectra in the dataset, see Extended Data Fig. 1b). **b**, Occurrences ('counts') of resolved mass lines and 'flank' peaks in 64 high-quality HMOC spectra. In contrast to the spectrum shown in **a**,

the histogram makes no distinction of the peak amplitude and shows only the frequency of occurrence of resolved mass lines. Above 80 u the characteristic HMOC mass lines appear, preceded by the peaks from benzene-derived cations at 77 u and 79 u. A peak that can be identified at around 95 u in some spectra is in agreement with phenyl cations ($C_6H_5^+$, 77 u) forming a water cluster ($C_6H_5–H_2O^+$), preferentially at lower-impact speeds (Extended Data Figs. 1, 3). Organic mass lines below 45 u appear preferentially at odd masses, at 15 u, 27 u, 29 u, 39 u, 41 u and 43 u, indicating a preference for odd numbers of H atoms with the typical cationic hydrocarbon fragmentation fingerprint (CH_3^+, $C_2H_3^+$, $C_2H_5^+$, $C_3H_3^+$, $C_3H_5^+$ and $C_3H_7^+$). Although other interpretations for each individual line are possible (for example, HCN^+ (27 u), COH^+ (29 u) and CH_3CO^+ (43 u)), the overall pattern here suggests hydrocarbons or hydrocarbon fragments. In **b** all signatures with possible major contributions from inorganic species are colour-shaded as in **a** and marked by green triangles. In both panels, the absolute masses have an intrinsic uncertainty (absolute value) of ±1 u at 80 u and ±2 u at 180 u due to the limited calibration accuracy of the CDA in this high-mass regime. The mass intervals between peaks, however, are accurate to the integer level.

However, aliphatic fragmentation is also indicated by strong peaks at 27 u–29 u ($C_2H_{3,4,5}^+$) and 41 u–43 u ($C_3H_{5,6,7}^+$) and a less-pronounced peak at 15 u (CH_3^+). Mass lines at 55 u–57 u are in agreement with aliphatic C_4 species ($C_4H_{7,8,9}^+$), whereas aliphatic structures with more than four carbon atoms (for example, $C_5H_{9,10,11}^+$, with 69 u–71 u) are generally absent (Fig. 1).

Each spectrum also exhibits water-cluster cations of the form $H_3O(H_2O)_n^+$ (Fig. 1), typical for water ice impacts[14,17]. Evidently, an ice–organic mixture constitutes the bulk composition of these particles. Ion abundances are indicative of an organic fraction in ice grains up to the per cent level (Extended Data Fig. 7). Particle radii are mostly between 0.2 μm and 2 μm (Extended Data Table 1). Na^+ ions and
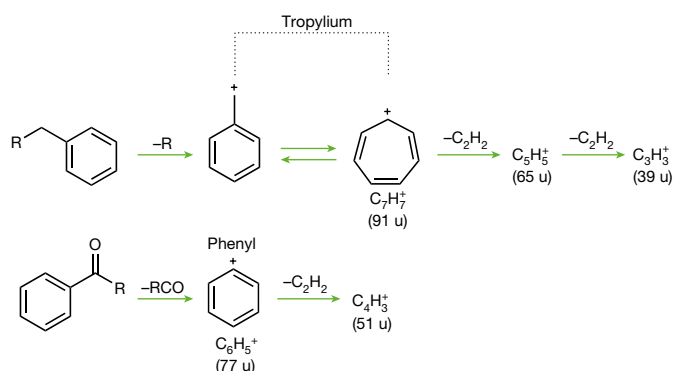
Fig. 2 | Formation of different aromatic cations. Although signatures in agreement with tropylium ions at ~91 u are present in every HMOC spectrum, they are on average about three times less abundant than the energetically favourable phenyl cation peak (Fig. 1a). If, upon breakup, the molecular structure allowed for an integration of a C–H group (top) into the highly stable aromatic resonance structure of the tropylium ion (91 u), then the formation of phenyl cations (77 u) would be suppressed (Extended Data Fig. 2). Only if the macromolecular structure does not allow this (bottom), phenyl (77 u) and benzenium (79 u, not shown) cations are the preferred single-ringed cations (also Extended Data Fig. 7). We note that fused benzene rings (such as PAHs) do not form either of these abundant single-ringed species (see Methods section 'Inferring the origin of HMOC peaks in CDA spectra' and Extended Data Fig. 8). Subsequent losses of neutral acetylene (C_2H_2) from phenyl and tropylium cations lead to smaller cationic fragments at 65 u, 39 u and 51 u[21], which are also seen in HMOC spectra (Fig. 1b).

sodium–water clusters ($Na(H_2O)_n^+$) appear in most HMOC spectra, but at a much lower level than in spectra of type-3 grains, which are thought to be generated from frozen spray of Enceladus' salty ocean[8,9]. In HMOC-type spectra the Na-to-water ratio is similar to the low abundance found in type-1 particles thought to condense from salt-poor water vapour[8,22].

Cassini's INMS has measured the integrated composition of the Enceladean plume at several flyby speeds[12]. In contrast to the CDA, which records cations that form upon impact, the INMS simultaneously measures the composition of neutral gas entering the instrument aperture and volatile neutral molecules that are generated upon the impact of ice grains onto the instrument's antechamber[23] (see Methods, 'INMS data analysis'). There is a striking overabundance of organic species in spectra obtained at high flyby speeds (14–18 km s^{-1}) compared to those obtained at slower velocities (7–8 km s^{-1}) that we attribute to fragmentation of large organic parent molecules beyond the upper INMS mass limit of 99 u (Fig. 3). Given the low temperatures, species above 99 u are expected to be extremely depleted in the plume gas and originate from ice grains, probably of HMOC-type, entering the INMS aperture at high speed.

Mass lines at 77 u–78 u stand out, in full agreement with the CDA's inference of benzene species. Because these are only apparent at high flyby speed, they cannot stem from benzene itself but, like the other species in the residual spectrum, must be fragments from larger parent molecules. As in the case of the CDA, some of the smaller require oxygen-bearing fragments. Further INMS compositional analysis of signals extracted explicitly from ice grain impacts (see Extended Data Fig. 10 and Methods section 'INMS ice grain spectrum') provides further evidence that CO is the dominant fragment species at 28 u and that a N-bearing fragment (C_2H_3N) might be present.

Despite the relatively low mass range and resolution of the Cassini mass spectrometers, the measurements lead to the following key constraints. (1) The HMOC pattern in the CDA spectra and the extended spectra support the presence of organic molecules with masses clearly above 200 u. (2) The typical spacing of 12 u–13 u between HMOC peaks implies unsaturated cationic fragments with a ratio of C/H ≈ 2. Impact
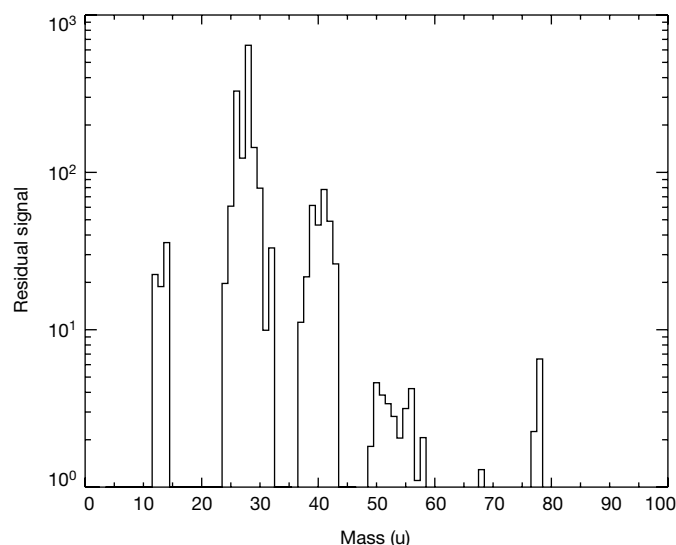
Fig. 3 | INMS organic fragmentation spectrum. By subtracting a plume-integrated INMS mass spectrum acquired at low velocities from a high-velocity spectrum, we obtain this residual signal (in arbitrary units), which we attribute to breakup products from high-mass species beyond the INMS mass limit at 99 u (Methods 'Residual spectrum from fast versus slow flybys'; Extended Data Fig. 11). Abundances of these high-speed fragments are normalized to the abundance of CH_4 (via its CH_3^+ ion at 15 u, which therefore has no signal in the residual spectrum). The species at 77 u and 78 u match the benzene-derived cations at 77 u and 79 u in the CDA spectrum. In contrast to the CDA, the INMS measures the composition of the neutrals and thus the neutral benzene ring (78 u) is expected to have the strongest signal in this spectrum. Many of the more abundant low-mass species are in agreement with aromatic fragmentation and oxygen-bearing parent molecules. Additional mass lines only seen at high-speed flybys (50 u–56 u) and much elevated signals in other masses (37 u–42 u and 25 u–28 u) indicate the unsaturated fragments C_4H_{2-8}, C_3H_{1-6} and C_2H_{1-4}, consistent with aromatic breakup products. Aliphatic fragmentation is required for the high-mass end of the C_2 and C_3 regions (29 u–30 u and 43 u). The overabundance at 28 u (CO), 30 u (probably H_2CO) and 31 u (probably CH_3OH) requires a contribution of oxygen-bearing fragments, consistent with CDA observations.

experiments with polystyrene[18,19] (Extended Data Fig. 2) indicate that the C/H ratio of the parent molecules might be lower (C/H ≈ 1) than in these fragments. (3) Prominent benzene-like species in the CDA and INMS spectra indicate the presence of abundant sub-structures of isolated benzene rings. From the INMS spectra, these features cannot originate from benzene itself, but are fragments of larger molecules. However, polycyclic aromatic hydrocarbon (PAH)-like fused rings do not form such fragments. Although not unique, the most parsimonious interpretation of these results is that these aromatic structures are parts of the same massive parent molecules that are responsible for HMOCs, which would explain their unsaturated nature. (4) From the suppressed formation of tropylium cations observed in the CDA spectra, we conclude that the rings are either connected to functional groups without carbon atoms or to dehydrogenated carbon atoms. (5) Unsaturated species at low masses are in close agreement with aromatic fragmentation. Aliphatic cations indicate saturated aliphatic structures with one to four C atoms arranged in parallel with the unsaturated (aromatic) structures. (6) Oxygen-bearing species in both the CDA and INMS spectra probably originate from hydroxyl, ethoxy or carbonyl functional groups. Nitrogen-bearing species are in good agreement with some features but do not provide a unique interpretation. Although no indication of other elements is observed in the organic structures, these cannot be ruled out.

Fragmentation of a single type of macromolecule may be responsible for all mass lines in the HMOC spectra. The parent substance would then be composed of cross-linked or polymerized aromatic and

aliphatic substructures with functional groups containing oxygen and probably nitrogen. Alternatively, contributions from lower-mass species might be mixed with macromolecules.

The Enceladean origin of these macromolecules is evident (see Methods sections 'Enceladus as the origin of HMOC parent molecules and exclusion of other potential sources' and 'Contamination of INMS spectra from previous measurements is unlikely'), and there is a multitude of speculative options for the genesis of these complex organics on Enceladus, some of which are outlined in Methods section 'Possible precursor scenarios for the observed complex organics'. However, the data do provide evidence of the formation of highly organic-enriched ice grains under quite specific conditions. Ice grains of very different salinity emerging from Enceladus have previously been identified in CDA mass spectra. Nearly pure water ice grains (type 1) can form from condensation of supersaturated vapour inside and above the ice vents[8,22,24]. In contrast, salt-rich ice grains (type 3) are thought to be frozen ocean spray[8,9], generated when bubbles of volatile gas (CO_2[25], CH_4 or H_2[12]) reach the water table and burst[26]. The HMOC-producing organic material (see Methods, 'Enceladus as the origin of HMOC parent molecules and exclusion of other potential sources') is detected in type-2 salt-poor ice grains, and thus cannot have formed directly from the salty ocean spray that preserves the composition of ocean water upon flash freezing[9]. Consequently, the observed organic compounds were not dissolved in ocean water when incorporated into ice grains. However, molecules with masses much larger than 200 u should not exist in the gas phase near the water table ($T \leq 0\,°C$); hence, the organic substances cannot have condensed from the vapour either, and must have been solid when the grains formed.

The most plausible way to generate the observed grains is if the organic material exists as a separate phase, such as a thin film or layer of mostly refractory, insoluble organic species on top of (at least parts of) the oceanic water table located inside water-filled cracks in the ice crust (see Extended Data Fig. 12 and Methods section 'Deduction of an organic enriched layer at the Enceladean water table'). Bursting bubbles then disperse the organic film and, besides salty water droplets, produce droplets or flakes of organic material. When ascending in the icy vents, the organics become coated by water ice condensing from the vapour carrying the grains (Extended Data Fig. 12). Indeed, the limited tendency of benzene cations in HMOC spectra to cluster with neutral water molecules disfavours intimate mixing of organics with water and implies a core–shell grain structure. In a well mixed system, such a cluster at 95 u is much more pronounced (Extended Data Fig. 7).

Aerosol formation from bubble bursting is a well studied process in Earth's oceans, which are covered by an organic microlayer[26]. Organic-bearing sea spray serves as highly efficient nucleation cores of ice clouds over polar waters on Earth[27] and is found preferentially in the smallest aerosols, between 40 nm and 250 nm in size[26,28], whereas larger aerosols with sizes between 500 nm and 1,000 nm are either organics mixed with salt or do not contain organics[29]. Under Enceladus' low-gravity conditions, one would expect larger gas bubbles and therefore larger film drops. Spectra showing HMOCs are generated by ice grains with radii of around 1 μm (Extended Data Table 1). The presence of insoluble organic nucleation cores, a few hundred nanometres in size, would naturally explain the high organic content in HMOC grains. Larger, organic-free salty ocean droplets account for the salt-rich type-3 particles detected by the CDA. Bubbles ascend through tens of kilometres of ocean before reaching the surface. Like in Earth's oceans, organic substances can accumulate efficiently on the bubble walls[30], thus probing the oceanic organic inventory at depth (see Methods, 'Deduction of an organic enriched layer at the Enceladean water table').

Online content

Any Methods, including any statements of data availability and Nature Research reporting summaries, along with any additional references and Source Data files, are available in the online version of the paper at https://doi.org/10.1038/s41586-018-0246-4.

1. Thomas, P. C. et al. Enceladus's measured physical libration requires a global subsurface ocean. *Icarus* **264**, 37–47 (2016).
2. Iess, L. et al. The gravity field and interior structure of Enceladus. *Science* **344**, 78–80 (2014).
3. Spencer, J. R. et al. Cassini encounters Enceladus: background and the discovery of a south polar hot spot. *Science* **311**, 1401–1405 (2006).
4. Spahn, F. et al. Cassini dust measurements at Enceladus and implications for the origin of the E ring. *Science* **311**, 1416–1418 (2006).
5. Porco, C. C. et al. Cassini observes the active south pole of Enceladus. *Science* **311**, 1393–1401 (2006).
6. Waite, J. H. Jr et al. Cassini ion and neutral mass spectrometer: Enceladus plume composition and structure. *Science* **311**, 1419–1422 (2006).
7. Hansen, C. J. et al. Enceladus water vapor plume. *Science* **311**, 1422–1425 (2006).
8. Postberg, F. et al. Sodium salts in E-ring ice grains from an ocean below the surface of Enceladus. *Nature* **459**, 1098–1101 (2009).
9. Postberg, F., Schmidt, J., Hillier, J., Kempf, S. & Srama, R. A salt-water reservoir as the source of a compositionally stratified plume on Enceladus. *Nature* **474**, 620–622 (2011).
10. Hsu, S. et al. Ongoing hydrothermal activities within Enceladus. *Nature* **519**, 207–210 (2015).
11. Sekine, Y. et al. High-temperature water-rock interactions and hydrothermal environments in the chondrite-like core of Enceladus. *Nat. Commun.* **6**, 8604 (2015).
12. Waite, J. H., Jr et al. Cassini finds molecular hydrogen in the Enceladus plume: evidence for hydrothermal processes. *Science* **356**, 155–159 (2017).
13. Choblet, G. et al. Powering prolonged hydrothermal activity inside Enceladus. *Nat. Astronomy* **1**, 841–847 (2017).
14. Postberg, F. et al. The E ring in the vicinity of Enceladus. II. Probing the moon's interior—the composition of E-ring particles. *Icarus* **193**, 438–454 (2008).
15. Waite, J. H. Jr et al. Liquid water on Enceladus from observations of ammonia and ^{40}Ar in the plume. *Nature* **460**, 487–490 (2009); corrigendum **460**, 1164 (2009).
16. Kempf, S., Beckmann, U. & Schmidt, J. How the Enceladus dust plume feeds Saturn's E ring. *Icarus* **206**, 446–457 (2010).
17. Postberg, F. et al. Discriminating contamination from particle components in spectra of Cassini's dust detector CDA. *Planet. Space Sci.* **57**, 1359–1374 (2009).
18. Goldsworthy, B. J. et al. Time of flight mass spectra of ions in plasmas produced by hypervelocity impacts of organic and mineralogical microparticles on a cosmic dust analyser. *Astron. Astrophys.* **409**, 1151–1167 (2003).
19. Srama, R. et al. Mass spectrometry of hyper-velocity impacts of organic micro grains. *Rapid Commun. Mass Spectrom.* **23**, 3895–3906 (2009).
20. Silverstein, R. M., Webster, F. X. & Kiemle, D. J. *Spectrometric Identification of Organic Compounds* 7th edn, 1–70 (John Wiley and Sons, Hoboken, 2005).
21. Dass, C. *Fundamentals of Contemporary Mass Spectrometry* 1st edn 210–238 (John Wiley and Sons, Hoboken, 2007).
22. Schmidt, J., Brilliantov, N., Spahn, F. & Kempf, S. Slow dust in Enceladus' plume from condensation and wall collisions in tiger stripe fractures. *Nature* **451**, 685–688 (2008).
23. Teolis, B. D., Perry, M. E., Magee, B. A., Westlake, J. & Waite, J. H. Detection and measurement of ice grains and gas distribution in the Enceladus plume by Cassini's ion neutral mass spectrometer. *J. Geophys. Res.* **115**, A09222 (2010).
24. Yeoh, S. K., Chapman, T. A., Goldstein, D. B., Varghese, P. & Trafton, L. M. On understanding the physics of the Enceladus south polar plume via numerical simulation. *Icarus* **253**, 205–222 (2015).
25. Matson, D. L., Castillo-Rogez, J. C., Davies, A. G. & Johnson, T. V. Enceladus: a hypothesis for bringing both heat and chemicals to the surface. *Icarus* **221**, 53–62 (2012).
26. de Leeuw, G. et al. Production flux of sea spray aerosol. *Rev. Geophys.* **49**, RG2001 (2011).
27. Wilson, T. W. et al. A marine biogenic source of atmospheric ice-nucleation particles. *Nature* **525**, 234–238 (2015).
28. Leck, C. & Bigg, E. K. Comparison of sources and nature of the tropical aerosol with the summer high arctic aerosol. *Tellus B* **60**, 118–126 (2008).
29. Gantt, B. & Meskhidze, N. The physical and chemical characteristics of marine primary organic aerosol: a review. *Atmos. Chem. Phys.* **13**, 3979–3996 (2013).
30. Porco, C. C., Dones, L. & Mitchell, C. Could it be snowing microbes on Enceladus? Assessing conditions in its plume and implications for future missions. *Astrobiology* **17**, 876–901 (2017).

Competing interests The authors declare no competing interests.

Additional information
Extended data is available for this paper at https://doi.org/10.1038/s41586-018-0246-4.
Reprints and permissions information is available at http://www.nature.com/reprints.
Correspondence and requests for materials should be addressed to F.P.
Publisher's note: Springer Nature remains neutral with regard to jurisdictional claims in published maps and institutional affiliations.

METHODS

CDA data analysis. *Short description of the CDA's chemical analyser subsystem.* The chemical analyser is the subsystem of the CDA[31] that provides chemical information about an impacting dust particle. Depending on its trajectory, the particle either hits the central rhodium target (chemical analyser target, CAT; diameter, 0.17 m), the surrounding gold target (diameter, 0.41 m) or the inner wall of the instrument. This work only deals with impacts on the CAT. If a dust particle impacts the CAT with sufficient energy, it becomes totally vaporized and partly ionized, forming an impact plasma consisting of target and particle ions, together with electrons and neutral molecules and atoms. The instrument separates this plasma, the positive component of which is linearly accelerated towards a multiplier about 19 cm away from the CAT, which is used to generate a TOF spectrum. The spectrometer is sensitive to positive ions only. The mass resolution, $m/\Delta m$, which is derived from laboratory experiments with the instrument, depends on the atomic masses of the ions. At 1 u, $m/\Delta m$ is 10, increasing to $m/\Delta m = 30$ at 100 u and up to $m/\Delta m = 50$ at 190 u—although these values vary strongly with impact conditions.

Acquisition of a spectrum in the high-rate sampling mode of the multiplier can be triggered by charge thresholds being exceeded on either the CAT or the multiplier. In the latter case, recording can be triggered up to several microseconds after the actual impact by the arrival of an abundant ion species; for water-dominated particles, these generally are hydrogen cations (H^+) or hydronium ions (H_3O^+). If triggered by the arrival of H_3O^+, mass lines of species with masses lower than 19 u, as well as the hydronium signature itself, do not appear in the spectrum. In this work, all spectra were triggered either directly by impact or by registering the H^+ signal at the multiplier.

The spectra are logarithmically amplified, digitized at 8-bit resolution and sampled at 100 MHz for a period of 6.4 µs after the trigger. The recording period of the high-rate sampling mode allows the detection of ions with masses of up to approximately 185 u, assuming that instrument recording is triggered by the impact itself, and about 215 u when recording is triggered by H^+. The acquisition of the extended spectrum starts after the high-sampling mode ends at 6.4 µs and is recorded with a sampling rate of 10 MHz up to a total time of 40 µs. The low number of data points corresponds to an extremely low mass resolution in the extended spectrum: one data point interval represents 7 u at 300 u and 20 u at 2,000 u. The extended spectrum frequently shows an instrument-artefact peak at 6.8 µs, which is ignored in our analysis.

Since the TOF is proportional to the square root of the mass-to-charge ratio of ions, in the ideal case its spectrum also represents a mass spectrum for identical ion charges. The ions created by impact ionization in the impact speed regime considered here (4–18 km s^{-1}) are almost exclusively singly charged. Unfortunately, the TOF is also influenced by the broad distribution of initial ion velocities, slightly varying flight paths and plasma shielding effects[32]. For that reason, species with identical masses are distributed over a range of sampling points and the mass resolution drops below integer values usually around 25 u–30 u. Therefore, we prefer to display original CDA spectra using a horizontal axis that shows the TOF, not the mass. The latter could incorrectly suggest an unrealistically high accuracy.

For a detailed description of the instrument, see Srama et al.[31]. The calibration routine is described in Postberg et al.[14,33]. For the dataset used in this work the calibration was done by using water and sodium mass lines, and a stretch factor of $a = 474$ ns was applied.

Dataset. All data used in this work are listed in Extended Data Table 1 and, like all CDA data, are archived on the Small Bodies Node of the Planetary Data System (PDS-SBN), at http://sbn.psi.edu/archive/cocda. We used 15 periods with good pointing of the CDA towards the E-ring dust ram direction between 2004 and 2008. This early period was chosen because there was negligible CDA contamination from salts deposited on the CDA impact target during deep Enceladus plume dives[17]. These 15 following periods (expressed in seconds), as recorded by the spacecraft clock, are:
1,477,548,025–1,477,746,968
1,489,004,979–1,489,118,561
1,498,469,760–1,498,505,448
1,506,223,870–1,506,436,625
1,509,311,996–1,509,357,627
1,511,686,278–1,512,480,582
1,514,090,477–1,514,186,815
1,515,560,669–1,516,328,727
1,519,522,033–1,519,612,908
1,521,596,023–1,522,361,262
1,543,798,083–1,543,831,204
1,544,838,694–1,544,916,311
1,557,517,652–1,557,520,425
1,589,065,736–1,589,083,623
1,605,559,719–1,605,566,052

Within these periods, a total of 7,353 spectra of impinging E-ring grains were investigated. A Lee filter was applied for better signal-to-noise ratio. Within the group of organic-bearing spectra (type 2[8,9,14]) we find a subgroup of spectra with a pattern of repetitive non-water peaks above 80 u (Fig. 1). We attribute this spectral pattern to HMOCs. The selection criteria are the following.

(1) At least five roughly well defined, equidistant peaks above 80 u with a signal-to-noise significance greater than 2σ.

(2) Water cluster peaks of the form $(H_2O)_n X^+$ (where X^+ is H_3O^+ or Rh^+, for example) are explicitly not considered for selection. Cases in which an HMOC pattern could be verified despite interference with water clusters were selected, but not considered for the sub-selection high-quality spectra (see Methods, 'Selection of 64 high-quality spectra for Fig. 1 and Extended Data Figs. 1 and 3').

(3) Isolated or irregular peaks above 80 u are not considered.

The much wider group of CDA type-2 grains[14] includes a multitude of organic-bearing ice grains observed in the plume and in the E ring. Other type-2 spectra not belonging to the type-2 subtype displaying HMOC patterns are outside the scope of this work.

Relative frequency of HMOC-type grains depends on impact speed and distance to Enceladus orbit. We find 83 spectra (1.1%) with apparent HMOCs, equivalent to about 3% of all type-2 spectra in the dataset (Extended Data Table 1). However, the probability of HMOC detection depends on the impact speed and thus the energy densities that the organic-bearing ice particles were exposed to upon impact. At high speeds (8–15 km s^{-1}) the overall frequency of HMOC detection is about 3% of all particles (~10% of type-2 spectra). At 6–8 km s^{-1} the HMOC detection frequency drops sharply to about 1% and goes down to 0.4% between 5 km s^{-1} and 6 km s^{-1} (see Extended Data Table 1). Below 5 km s^{-1} no HMOC was detected, equivalent to a probability of less than 0.1%. In the few spectra in the dataset recorded at speeds above 15 km s^{-1}, no HMOCs were detected (equivalent to a probability of <1.7%), so the speed range 8–15 km s^{-1} seems to be optimal for the CDA to record HMOC spectra. At speeds below 8 km s^{-1} the probability to produce fragments from the proposed parent molecules (outside the CDA mass range) decreases and becomes close to zero below 5 km s^{-1}. At speeds above 15 km s^{-1} the detection probability seems to decrease again, probably because at these high-impact speeds mostly small fragments with masses <80 u are produced, whereas the production of fragments that yield the typical HMOC pattern between about 80 u and 200 u (the defining feature of this CDA spectrum type) becomes less likely.

HMOC grains were detected in the plume (Extended Data Fig. 6) and in the E ring in a wide range of Saturnian distances from $3.8R_S$ to $14R_S$, where R_S is Saturn's radius, except in its outermost fringe, which extends[34] out to $20R_S$. However, the fraction of HMOC-type grains in the E ring increases closer to Enceladus' orbit. The chance to encounter an HMOC grain with intermediate impact speed of 6–8 km s^{-1} is about 2.5% at a Saturnian distance of $3.8R_S$–$5R_S$ and drops to 1.5% at $5R_S$–$7R_S$. Beyond $7R_S$, the detection probability decreases sharply to 0.5% and is 0.3% beyond $11R_S$. This clearly points at an Enceladus origin (see 'Enceladus as the origin of HMOC parent molecules and exclusion of other potential sources').

The effects of speed and distance are cumulative: in the optimal speed window and close to the orbit of Enceladus, the detection rate is highest, at about 4%. Thus, we can conclude that the actual fraction of ice grains carrying substantial amounts of complex organic material ejected into the E ring is at least 4% of the grains in the size range covered by the CDA (grain radius $r \approx 0.2$–2 µm). An instrument with an extended mass range (for example, up to 2,000 u) and higher resolving power than the CDA would probably detect complex organics with similar or higher probability at encounter speeds of ~5 km s^{-1} with the organic parent molecules being largely intact.

Selection of 64 high-quality spectra for Fig. 1 and Extended Data Figs. 1 and 3. For the peak statistics and co-added spectra in Fig. 1 and Extended Data Fig. 3 and the semi-quantitative spectra depicted in Extended Data Fig. 1, we used a subset of 64 spectra that had the highest quality. The 19 spectra that were not selected either had:

(i) an extended water-cluster pattern (for example, $(H_2O)_n$–H_3O^+ or $(H_2O)_n$–Rh^+), where strong peaks overlapped with the HMOC region above 100 u, or

(ii) an HMOC pattern with a low signal-to-noise ratio and poor peak definition that did not allow a reliable quantification of all features, or

(iii) an irregular baseline (instrument artefact) that did not allow a reliable quantification and would have spoiled the quality of the co-added spectra, or

(iv) an uncertain calibration, which did not allow an unambiguous assignment of peak masses.

In cases (i) and (ii), the organic fraction in the ice grains is probably lower than in other HMOC spectra.

In Extended Data Fig. 3 the dataset is split into 'fast' and 'slow' impacts (above and below ~10 km s^{-1}, respectively). The fast co-added spectrum is composed of 12 of the 64 high-quality HMOC spectra recorded after an impact with a velocity higher than ~10 km s^{-1}. In this case the speed was determined by the presence of

one or more hydrogen cations (H^+, H_2^+, H_3^+). The uncertainty of this method is clearly below the uncertainty achieved when using assumptions on the orbital elements, shown in Extended Data Table 1. The appearance of H^+ cations is a reliable indicator of impact speeds[17,35] in excess of about 12 km s^{-1}, and H_2^+ and H_3^+ cations appear already at slightly lower speeds (>10 km s^{-1})[17]. For 12 spectra in which one or more of these hydrogen mass lines were present, this reliable speed threshold indicator was used. The remaining high-quality spectra were co-added to produce the slow spectrum in Extended Data Fig. 3. Owing to their higher kinetic energy upon impact, low-mass cationic fragmentation species are more abundant there. Moreover, fast spectra were on average triggered earlier, mostly directly after impact (see 'Short description of CDA's chemical analyser subsystem'). Therefore, the high-rate recording interval of 6.4 μs stopped at a lower equivalent mass than for the lower-speed spectra (Extended Data Fig. 1), and the HMOC peak at ~191 u was often not recorded for fast spectra.

Inferring the origin of HMOC peaks in CDA spectra. In the main text we argue that the HMOC pattern is indicative of highly unsaturated organic cations. A very similar pattern was also observed in CDA ground calibration experiments that used a dust accelerator[36] to produce impacts from micrometre-sized polystyrene beads (see figures 10 and 13 in Goldsworthy et al.[18]). The accelerator experiment was later repeated using an advanced TOF dust analyser with higher mass resolution[19] (Extended Data Fig. 2), giving identical results. A similar, but not identical, unsaturated cationic fragmentation pattern was observed in TOF-SIMS (secondary ion mass spectrometry) experiments with polystyrene[37]. The most plausible explanation for the fragmentation pattern and the ionic species observed is given in table 2 of ref. [37]. Although the spacing of 12.5 u in the HMOC pattern seems to suggest a C/H ratio of 2 or even higher, all three polystyrene experiments show that such an unsaturated cationic fragmentation pattern can also be achieved with parent molecules with a C/H ratio of only 1. These analogue experiments demonstrate that the C/H ratio of the cationic fragments could be different from that of the bulk material.

However, there is a noticeable difference between polystyrene spectra and HMOC spectra: in contrast to HMOC spectra, tropylium ions (91 u) form abundantly in impact ionization polystyrene spectra, whereas phenyl cations (77 u and 79 u) are relatively depleted. In Fig. 2 we demonstrate the reason: in polystyrene, polymer alkyl groups are attached to each of the aromatic monomers, which allow easy formation of tropylium ions at 91 u (Extended Data Fig. 2). This is also known from classical electron ionization mass spectrometry: abundant phenyl cations form only if the formation of tropylium ions is sterically difficult or impossible[20,21]. This leads to our conclusion that for HMOC parent species, single-ringed substructures are predominately attached to dehydrogenated carbon atoms or to functional groups without carbon.

In the dust accelerator experiments with polymers, an HMOC-like pattern was observed at impact speeds[18,19] of 4–6.5 km s^{-1}. Above this speed further fragmentation occurred. By contrast, CDA HMOC spectra are observed at impact speeds of about 5–15 km s^{-1}. The water ice matrix in which the HMOC parent molecules are embedded might explain this difference. It is well known from matrix-assisted laser desorption/ionization experiments that water protects large organic molecules from fragmentation very efficiently.

An alternative interpretation of the origin of HMOCs might be very large PAHs. However, in our laser-assisted analogue experiment with pyrene in a water matrix (see Extended Data Figs. 8, 9 and Methods section 'Laser dispersion analogue experiments for icy dust impacts'), we do not observe efficient fragmentation of the PAH. These findings generally agree with information from electron ionization (70 eV) mass spectrometry of a wide range of PAHs. By contrast, Stephan et al.[38] demonstrated a pattern similar to the one observed with the CDA above 100 u using TOF-SIMS of a mixture of high-mass PAHs. However, the applied energies were much higher (25 keV) and the PAHs were not embedded in a water matrix, which naturally protects organic molecules from breakup[39]. In any case, regardless of fragmentation at harsh ionization conditions, PAHs do not yield any monoaromatic peaks; hence, neither phenyl (77 u) nor tropylium (91 u) cations form[40]. Therefore, if PAHs have a role in the origin of HMOCs, other parent molecules must be responsible for the strong monoaromatic peak in the CDA and INMS spectra.

In principle, monoaromatic cations in the CDA spectra (77 u, 79 u) could originate from benzene mixed within the macromolecular structure responsible for the HMOCs. However, this is not possible for the benzene feature (78 u) seen in the INMS spectra because they exclusively appear at high-speed flybys and thus must be fragments of larger molecules. It is plausible that the monoaromatic features observed in both instruments originate from HMOC-type ice grains (see next section) and therefore also in CDA spectra we consider molecular fragmentation as the most likely source.

INMS data analysis. *Residual spectrum from fast versus slow flybys.* The INMS[41] measurement routinely integrates the composition of plume gas over the flyby to increase the signal-to-noise ratio. Using this methodology, volatile compounds

released from ice grains that fragment and evaporate upon impact onto the instrument's antechamber[23] cannot be discriminated. In contrast to the CDA, which records cations, the INMS observes volatile neutral molecules that are in the vapour phase or are generated by ice grain impacts in the plume, and are subsequently ionized by the impact of 70-eV electrons in the ion source.

The residual spectrum presented in Fig. 3 represents the difference in composition and overabundance of organic material observed by the INMS during high-velocity flybys compared to low-velocity flybys through the Enceladus plume (Extended Data Fig. 11). Our interpretation of this spectrum is that low-speed flybys result in minimal fragmentation of the organic compounds within the ice grains. By contrast, high-speed impacts lead to fragmentation of large organic parent molecules beyond the INMS mass range of 99 u. Species with molecular masses above 99 u in the plume are expected to be extremely depleted in the gas phase and have to reside inside or on the ice grains. Based on the knowledge of the compositionally different ice grain populations that the CDA has collected over many years, HMOC-type grains entering the INMS's aperture are the most plausible source. The similarity in the composition of the fragments seen by the CDA and the INMS reinforce this assertion.

To obtain the spectrum shown in Fig. 3 we took the summed spectrum of the E5 flyby[15] and subtracted the average summed spectrum of the E14, E17 and E18 flybys. These represent the fastest (E5 at ~18 km s^{-1}) and slowest (E14, E17 and E18 at ~8 km s^{-1}) flybys through the plume for which the INMS has the best data. The three slow flybys have been combined into an average spectrum to compensate for their lower signal-to-noise ratio. Velocity-driven processes complicate the spectral comparison. H_2O–Ti reactions in the INMS antechamber increase with velocity owing to vaporization of Ti from the walls of the instrument's antechamber and create excess H_2 from H_2O, leaving TiO and TiO_2 as by-products[15]. Likewise, CO_2 fragments to become CO more readily as the velocity increases. Lastly, fragmentation products of high-mass organics probably enhance the plume gas signal for all masses dominated by organics in the INMS mass range. This makes it difficult to set an accurate reference point with which to compare the high- and low-velocity spectra. We have chosen to use the signal at 15 u in both the high- and low-velocity spectra as the common reference point because the CH_3^+ dissociative ion from CH_4 dominates the signal at this mass; furthermore, CH_4 is considered to be a plume-derived volatile species not considerably altered by fragmentation of high-mass organics. Choosing a mass of 15 u as the common reference point removes all the signals at this mass for the residual spectra, whereas in all other masses the signal is positive or negative. After matching the two spectra at their 15 u signal (Extended Data Fig. 11) and subtracting the low-velocity spectrum from the high-velocity spectrum, we set the amplitude scale of the residual relative to the noise floor of the low-velocity flybys (about 5 orders of magnitude lower than the H_2O signal at 18 u) so that only residual signal with a high signal-to-noise ratio is visible. The residual signal presented in Fig. 3 can be considered to be a conservative estimate of the high-mass organic fragmentation effect; if the CH_4 in the high-velocity flyby was increased from the low-velocity flybys, the residual signal would be even larger in amplitude.

Hydrocarbon species observed in this conservative estimate of the residual signal are discussed in the main text. Moreover, the residual spectrum suggests that at least 50% of the 28 u peak is from CO, given the upper limits placed upon N_2 and C_2H_4 in the fast E5 spectrum[15]. Oxygen-bearing species H_2CO and CH_3OH are suggested as the likely sources of the residual signal at 30 u and 31 u because they are the dominant species for these peaks in the E5 spectrum[15] and the residual retains more than 60% of the original E5 signal. This interpretation is strongly supported by the INMS ice grain spectrum.

INMS ice grain spectrum. To isolate spectral signals from icy grains when crossing the plume, we extracted those parts of the high-time-resolution, real-time INMS plume spectra (every 2.3 s) that registered the ice grains as spikes in the closed-source neutral (CSN) data[23,42]. The quadrupole mass analyser has a mass step integration period of 34 ms, whereas the vaporized gas from the impact dissipates in the antechamber in less than 3 ms. Therefore, the ice impacts appear as gas bursts or 'spikes' superimposed on the smoothly varying gas spectra that are mass-filtered by the mass step of the analyser. Thus, each spike can register only one unity-mass location per ice impact. By summing the spikes over three similar encounters (E14, E17 and E18) there are sufficient mass sampling statistics over the full sampled mass range to construct a pseudo-mass spectrum that represents the composition of the micrometre-sized grains.

Extended Data Fig. 10 shows this pseudo-mass spectrum of the grains measured by the INMS within 100 s of the time of closest approach. Each of the three encounters provided approximately 200 individual measurements or spikes to the composite spectrum. The vertical axis represents the relative count rate for each mass, because the counts for each mass are adjusted for the number of measurement opportunities (integration periods) for each mass. The scale of the plot is adjusted so that the minimum count rate is 1 count per integration period. The dispersion in the measurements obtained in the three encounters represents

the uncertainty on the count rates. The grain measurements are heavily concentrated near the closest approach, peaking with more than one spike per every ten integration periods at 2 u, which is the mass most sensitive to the grains. Analysis of the ice grain spectrum reveals a composition related to, but distinct from, the plume gas.

Two observations are particularly relevant to the high-mass organic material presented in this work (Extended Data Fig. 10). First is the clear dominance of CO at 28 u and the lack of N_2. By applying the well known quantities of dissociative species from the impact of 70-eV electrons in the INMS ionization chamber, CO_2 accounts for ~3% of the 28 u signal. N_2 has an upper limit of ~10% of the 28 u signal owing to the low signal at 14 u (N^+ dissociative ion) and may not be present at all. If present, C_2H_4 is limited to less than ~6% of the 28 u signal. This leaves a requirement for CO to be the dominant species at 28 u, which matches well the signal at 12 u and 14 u (C^+ and CO^{++} dissociative peaks). Although not a unique source, CO may be released from carbonyls in HMOC parent compounds by decarbonylation reactions during high-speed impacts of ice grains in the INMS. The caveat here is that the INMS integrates over all ice grains detected in the plume. Therefore, CO from carbonates or bicarbonates found in type-3 grains[9,11] might contribute here as well. The second observation is the likely presence of C_2H_3N. The signal pattern at 39 u–42 u suggests a species with its highest signal peak at 41 u and lower signal in the surrounding masses. C_2H_3N is the best candidate because it matches this 'stair step' pattern extremely well. C_2H_3N also appears to be present in the plume gas spectra, possibly because of contamination from a distribution of small grains indistinguishable from the incoming gas.

We note that in contrast to the spectrum in Fig. 3, these ice grain spectra were recorded at slow flyby speeds and show no signal with sufficient signal-to-noise ratio above 50 u. Unfortunately, ice grain spikes at the high-velocity flyby (E5) are not abundant enough to compose a similar spectrum, as shown in Extended Data Fig. 10.

Deduction of an organic enriched layer at the Enceladean water table. The observation of high concentrations of solid material in a water ice matrix that does not represent the ocean's salinity but is emitted from a saline ocean source, requires specific conditions during the formation of these grains. Because of the low temperatures near the water table where the ocean water is in contact with the ice crust, we conclude that the HMOC parent species are solid. The fact that the organics are embedded in a salt-poor water ice matrix indicates that they mostly are poorly soluble in water. In principle, primordial refractory organic substances trapped in the ice crust near the cracks, which become mobilized by the ascending vapour, could serve as an organic source. However, we disfavour this scenario because the crack walls are continuously coated by fresh ice condensing from the vapour flow[43,44].

We rather promote a scenario that is well known from ice cloud formation over polar waters on Earth[27]. There, organic aerosols of mostly biogenic origin[26] produced by bubble bursting serve as highly efficient nucleation seeds. When bubbles burst on Earth's oceans, an organic-free sea spray forms in parallel with pure organic aerosols and mixed phase organic-bearing sea spray[29,45]. The organic mass fraction of sea-spray aerosol has been consistently shown to be inversely related to aerosol size[29,46,47]. The purely organic end-members are found preferentially in the smallest aerosols[26,28] and are mostly water-insoluble[26,47]. As shown in the main text, the size of the organic nucleation cores in oceanic sea spray matches the CDA observation quite well.

Aerosol formation on Earth also provides a plausible analogue mechanism for the simultaneous production of salty ocean spray and organic aerosols: if the droplets are smaller than a few micrometres, then they can be thermally supported in water vapour with gas density slightly below the triple point against Enceladus' gravity. They do not fall back into the liquid, but are carried upwards through the ice vents by gas from evaporating water, following the pressure gradient into space. In parallel to the formation of smaller organic aerosols, larger salty ocean droplets form, which are later detected by the CDA as salt-rich type-3 particles in the plume and in the E ring. The analogue from Earth would also predict some larger mixed-phase particles that carry both ocean salts and complex organics, but these have not been identified by the CDA. One explanation could be that the macromolecular HMOC parent substance might be hydrophobic and would thus naturally avoid forming mixed-phase organic–sea-water aerosols.

On Earth, bubbles are generated mostly by breaking of waves[27]. On Enceladus, several volatile gases (CO_2, CH_4, NH_3 and H_2) have been detected in substantial concentrations in the plume[12] that will inevitably create bubbles when they rise though the ocean; these bubbles will then burst at the water table. In Earth's oceans, bubbles not only produce an aerosol, but are also very efficient in 'harvesting' organic molecules from the deeper oceanic environment by collecting these substances on their surfaces while ascending. The increase of relative organic concentrations observed near the surface of Earth's oceans by 2 to 3 orders of magnitude[48–50] suggests a selective transport of organic matter from the bulk seawater to the water table and then from the microlayer to atmospheric aerosols[27,29,51].

Possible precursor scenarios for the observed complex organics. There are many ways to explain the presence of complex organic materials in an icy moon in the outer Solar System. The two general categories of origin are accretion of primordial material and endogenic synthesis. In the former hypothesis, the organic carbon on Enceladus would predate the formation of the moon, and Enceladus would have acquired an organic inventory via its building blocks (icy planetesimals). The latter hypothesis would require hydrothermal systems inside Enceladus' porous rocky core[13] to produce complex organic molecules from small molecule precursors. This category can be broken down into several sub-categories characterized by molecular precursors. Organic compounds can be synthesized from more oxidized forms of carbon, such as CO_2, CO or formate[52,53]. More reduced simple organic species (formaldehyde, methanol and HCN) can also serve as feedstock for the synthesis of more complex organic compounds[54,55]. Methane is a relatively inert species, so it may be a less favourable carbon source, unless prolonged metamorphism or radiation chemistry is involved. Both abiotic and biotic processing of these precursors is possible. A mixture of spatially distinct (for example, ocean versus rocky core) sources is also not to be excluded at the present state of knowledge.

As an example of endogenic synthesis, relatively oxidizing hydrothermal conditions may promote the conversion of simple primordial organics into reactive unsaturated compounds, such as quinones, (poly)phenols or aldehydes, which may in turn polymerize (possibly in the presence of catalytic minerals) to form relatively hydrogen-poor macromolecules. Macromolecules on Enceladus that contain aromatic units with connecting short aliphatic chains that include more or less oxidized functional groups may resemble some humic substances on Earth. On Earth, several pathways exist for the formation of humic substances during the decay of biogenic complex organic matter[56]. However, these macromolecules may also be formed via synthetic routes, such as radical polymerization of phenolic compounds in the laboratory. Hänninen et al.[57] showed that humic acid-like polymers can be synthesized from homogeneous, well defined starting materials under oxidative conditions. The polymers display clear signatures of phenolic, aromatic (olefinic) and carboxyl carbons, and carboxyl carbons are present regardless of whether the monomeric unit possesses a free carboxyl group or not. On this basis, it was concluded that a partial de-aromatization occurs during the oxidative polymerization of o- and p-diphenolic compounds. Hänninen et al.[57] also reported that the ^{13}C nuclear magnetic resonance spectra and other features of the synthesized polymers resemble to a large extent the spectra of humic acids. The characteristics of these macromolecules are consistent with our observations from the HMOC spectra.

One can also consider a primordial origin of organic materials, which would be the simplest possibility. If the rocky materials that were accreted by Enceladus were analogous to CI-, CM- or CR-group chondrites or refractory cometary solids, then a substantial organic inventory is inescapable. CI chondrites in particular contain ~2 wt% insoluble organic carbon[58]. This insoluble organic matter (IOM)[59–63] is considered to be partly of primordial origin (that is, inherited from the interstellar medium) and partly modified by early hydrothermal processing on carbonaceous chondrite parent bodies. These asteroidal small bodies or planetesimals accreted within a few million years after the Solar System formation, heated up as a result of radioactive decay (mainly from ^{26}Al) and persisted at elevated temperatures, causing hydrothermal alteration and metamorphism for at least a few tens of millions of years after Solar System formation. While analytical data for comets are much more limited, recent results from comet 67P indicate a much higher organic carbon content of ~30 wt% in dust particles[64,65]. To put these extraterrestrial numbers into perspective, we note that hydrocarbon source rocks on Earth have an average total organic carbon value of ~2 wt%[66].

Enceladus organic matter may be similar to chondritic IOM. The latter shows some compositional variability: particularly in classes like CV and CO, which experienced strong thermal metamorphism at temperatures of about 400 °C–600 °C, both the H/C and O/C ratios are lower (down to 0.1 and 0.05, respectively), whereas in more primitive classes (CI, CM, CR) mild aqueous activity (100 °C–200 °C) prevailed and allowed the preservation of O/C ratios as high as 0.23 and H/C ratios[59] of 0.8. IOM in the CI, CM and CR classes is considered to be the most primitive type of IOM and has an average composition of $C_{100}H_{70}O_{22}N_3S_7$. It is macromolecular, and most of the carbon is incorporated in small aromatic structures, with about 20%–30% of the carbon constituting aliphatic bonds. The maximum length is 7 carbon atoms for aliphatic bridges between aromatic units and 4 carbon atoms for side chains with a free end[60,61]. Functional groups containing O, N and S are also abundant (see Fig. 2 in Remusat[61]). These characteristics are consistent with our observations from the HMOC spectra.

Because this subtype of IOM is thought to be the product of mild thermal and aqueous alteration, on the basis of present information it is impossible to say if this alteration already happened inside icy planetesimals under the influence of ^{26}Al heating or only later on Enceladus. There, under the influence of tens of millions of years of hydrothermal processing[13], more primitive primordial organics could have been transformed into a different organic mixture.

In the following, we will elaborate further on scenarios that invoke some level of processing of primitive organics on Enceladus. At a depth of about 60 km below the surface, the ocean comes in contact with Enceladus' core. The core's very low density ($\sim$2,500 kg m^{-3}) suggests $\sim$20% porosity[2,13]. Owing to the low pressures and modest temperatures in Enceladus' interior, an unconsolidated core with such porosities can be inherited from the accretion and differentiation process. Tidal forces help to maintain this fragmented state so that ocean water can percolate through it, up to the present day. In Enceladus' interior, temperatures of 100 °C or more (increasing towards the core centre) can be maintained over at least tens of millions of years. Depending on the permeability of the core, the entire ocean could be processed at temperatures higher than approximately 100 °C within[13] 25–250 Myr.

While primordial oxygenated and nitrogenous species, such as alcohols, carboxylic acids, amines and nitriles, may be more soluble in liquid water and can be leached into the subsurface ocean of Enceladus, larger polymeric organics would exist as a separate organic layer. If not heated above $\sim$300 °C, these organics might remain largely unaltered over geological timescales. Intense interaction with water, however, might have oxygenated the macromolecules on one end to form micellar structures (hydrophilic exterior and hydrophobic interior) and preserved their structural integrity over the lifetime of Enceladus.

Alternatively, a large accreted inventory of IOM-like material could establish the basis of a more evolved organic factory inside Enceladus' rocky core, similar to oil- and gas-generating sedimentary basins on Earth. To make this factory operational and enable consistency with the organic observations in the plume, organic compounds must be mobilized from source rocks. Hydrothermal activity[10,12] could facilitate this process. Cooking organic matter (metagenesis) in the core would crack it into smaller constituents, which may then be transported by fluid flow[13] as dissolved species, liquid droplets or entrained particulates (of particular relevance to the observations). A possible Earth analogue for this general scenario is Guaymas Basin in the Gulf of California[67]. This type of scenario has also been suggested for the interior of Pluto[68].

Is a scenario of processing primordial organic materials in Enceladus' core consistent with the chemical and structural features of compounds detected in the plume? Before proceeding, it is important to emphasize that it is still an open question whether we are seeing features that are representative of bulk organic materials in the subsurface. Processes that could fractionate organic compounds from their hypothesized source region to our instruments include expulsion from the core, (bio)degradation, hydrophobic phase separation in the ocean, plume outgassing and impacts during high-speed flybys. In light of these considerations, it seems prudent to focus on broad chemical characteristics.

Our data show the presence of unsaturated carbon and in particular the benzene ring. The former finding agrees qualitatively with elevated temperatures that promote entropically driven (more product than reactant molecules) dehydrogenation reactions. Countering this effect might be high concentrations of H$_2$ in hydrothermal fluids[12]; however, hydropyrolysis experiments demonstrate that aromatic carbon can coexist with abundant H$_2$[69]. The outcome on Enceladus presumably depends on the conditions of temperature and H$_2$ concentration, as well as the duration of heating and the availability of hydrogenation catalysts such as nickel. If primitive organic matter in chondrites[58] and comets[70] can serve as a guide, it can be expected that Enceladus would have accreted organic materials containing benzene rings. From the perspective of a primordial origin, it therefore makes sense to find the benzene ring as part of the organic structures at Enceladus. It is unknown how much thermal maturation has occurred, but complete graphitization can be ruled out because the presence of organic-bound hydrogen is implied by the data. This imposes a limit on the thermal history of the organic source rocks, which seems consistent with the persistence of a low-density core rich in hydrated silicates[2]. These organics have not been overcooked.

Two other compositional features are relevant to a general discussion. First, the likely presence of oxygen- and nitrogen-bearing functional groups is consistent with inheritance of these heteroatoms in accreted organic matter (O/C $\approx$ 0.2, N/C $\approx$ 0.04)[58,70] or their subsequent incorporation into organic structures by hydration or amination reactions (for example, of C=C or C≡C) on Enceladus. The latter processes would be facilitated by the availability of liquid water and ammonia in the interior[12]. Having heteroatoms also constrains the degree of thermal maturation. The second feature that we wish to highlight is the presence of methane in the plume[12]. It must be noted that there are multiple ways to explain the origin of methane[71], but it is appealing to envision a common mechanism for the formation of the full spectrum of organic compounds found at Enceladus. The analogy to petroleum geochemistry on Earth implies that thermal processing of organic materials will inevitably produce some CH$_4$ accompanying more complex organics[66]. The exact quantity of thermal gas will depend on the nature of the organic source material and the environmental (for example, redox) conditions. At Guaymas Basin, hydrothermal fluids have very high concentrations of CH$_4$ ($\sim$60 mmol kg^{-1})[72]. If the rocky core of Enceladus is also organic-rich and heated sufficiently, then this becomes a plausible scenario.

Enceladus as the origin of HMOC parent molecules and exclusion of other potential sources. *Photolysis in the E ring.* Most individual ice grains reside in the E ring for months to a few decades before they collide (either with a moon or the main rings) or before they are completely eroded by plasma sputtering. The oldest populations are generally located further away from their origin, Enceladus, in the outer E ring[73,74]. In principle, one has to consider that either HMOC parent molecules are not from Enceladus but evolved by photolysis from originally simple organics to the observed complex compounds in the E ring, or that the complex organics are from Enceladus but have been severely altered—for example, by dehydrogenation. However, several observations are not in agreement with these scenarios.

• The CDA observed a larger proportion of HMOC-type ice grains in the (young) inner E ring than in the (old) outer E ring (see Methods, 'Relative frequency of HMOC-type grains depends on impact speed and distance to Enceladus orbit'). This indicates degradation of the observed complex organics with time in the E ring, rather than their generation.

• During Cassini's E17 flyby, one freshly ejected HMOC-type ice grain was observed inside the plume (this was not included in the compositional analysis of this study, but it is shown in Extended Data Fig. 6). Furthermore, the CDA observed many HMOCs at locations close to Enceladus' orbit, where most grains had been ejected from the plume only a few days to few months ago.

• The INMS observations were directly made in the plume with freshly ejected material.

Instrument contamination. Intrinsic instrument contamination can be excluded as a source for the abundant organics in the spectra[17]. Of concern are the large PAHs in Titan's atmosphere, which may have deposited onto the surface of the CDA's impact target during close Titan flybys. Several pieces of evidence point against cross-contamination from Titan:

• The first HMOC spectra were already detected in 2004 and early 2005, before Cassini's first close flyby of Titan.

• The CDA has a decontamination device that was used between Titan flybys, which heats the CDA impact target to 100 °C for several hours.

• No buildup of organics can be observed in spectra of E-ring grains over time.

• The fact that only about 1% of impacts in the E ring show such a massive organic signature is not in agreement with a coating of organic contamination on the impact target.

• The trend to observe HMOC-type grains at a higher frequency closer to Enceladus' orbit than in the outer E ring (see 'Relative frequency of HMOC-type grains depends on impact speed and distance to Enceladus orbit') is not in agreement with a contamination origin.

• Thousands of spectra from impacts of dust populations outside the E ring (stream particles, exogenous dust and main-ring dust) never show HMOC features.

Contamination of INMS spectra from previous measurements is unlikely. The multiple environments encountered by the INMS require an evaluation of the potential for one environment to deposit refractory material onto the surfaces of the CSN antechamber and for that material to be released and measured at a later encounter. Of particular concern are the large PAHs in Titan's atmosphere and Enceladus' ubiquitous nanograins, which may fragment material deposited onto the antechamber surfaces, sputter the organic products, and thus release volatiles into the INMS.

The strongest evidence that high-speed nanoparticles do not create false signals in the INMS spectra is that the amounts of PAHs encountered at Titan are insufficient to produce the INMS measurements obtained during encounters such as E5. At Titan, both the INMS and the CAPS measure PAHs or their fragments, with benzene observed by both instruments. Waite et al.[75] and Lavvas et al.[76] analysed these measurements to estimate the abundance of PAHs as functions of altitude and of mass. Combining these estimates with the conservative assumption that every PAH molecule that enters the INMS CSN aperture during the Titan encounters is then released during E5, the resulting signal would be more than an order of magnitude below the level measured by the INMS at the fast Enceladus flyby (E5), as detailed in the following paragraph.

The benzene density in Titan's atmosphere is well modelled by an exponential with a scale height of 15–20 km and a density of approximately[75] 10^5 molecules per cubic centimetre at 950 km. Before E5, there were thirteen Titan encounters with the INMS pointed to accept atmospheric neutrals, and approximately 10^{11} higher-mass molecules entered the INMS CSN antechamber during those encounters. To produce the E5 measurements, the CSN antechamber maintained a density of less than 10^7 molecules per cubic centimetre for at least 40 s for the heavier species. With a residence time of only a few milliseconds, more than 10^{12} heavy molecules were required in the CSN antechamber during E5. The number of molecules encountered at Titan is thus at least a factor of ten below the number of molecules required in the CSN antechamber to produce the higher-mass count rates observed during E5.

There is further evidence that the INMS spectra are unaffected by previous encounters: the CSN spectra at Enceladus do not change over many years, despite scores of Titan encounters during that period. Furthermore, there is no apparent dependency of Enceladus' spectrum on whether a Titan encounter occurred between sequential Enceladus flybys.

Laser dispersion analogue experiments for icy dust impacts. Extended Data Fig. 9 shows a sketch of the experimental setup in Heidelberg. A liquid water beam, in which the tested substances are dissolved, is injected into a high vacuum $(5 \times 10^{-5} \text{ mbar})$ through a quartz nozzle (with opening radius 6–8 μm). The quartz nozzle is mounted on a three-axis manipulator. A high-performance liquid-chromatography pump (model 300c, Gynkotek) is used to keep the flow rate constant at 0.17 ml min^{-1}. The liquid beam flow is stable for ~3 mm downwards and then disintegrates into droplets. To maintain the high vacuum, the liquid pours into two liquid-nitrogen-cooled cryotraps. To perform the measurements, the water beam is hit by a pulsed infrared laser (Opolette HE 2731, OPOTEK; 20 Hz, 7 ns pulse length), which operates at a wavelength of approximately 2,850 nm and a pulse energy of up to 4 mJ. The laser is directed and focused onto the liquid by three CaF$_2$ lenses and a gold mirror. The wavelength is chosen to specifically excite the OH stretch of the water molecules. When the laser energy is absorbed by the water beam, the water is rapidly heated and disperses explosively into fragments. In this way cations, anions, electrons and neutral molecules are created[39,77].

Depending on the operation mode, cations or anions that pass through a skimmer are analysed in a reflectron TOF mass spectrometer (Stefan Kaesdorf). This mass spectrometer operates according to the principle of delayed extraction. The delay time is adjusted with the aid of a pulse generator (model DG535, Stanford Research Systems). By adjusting the delay time, ions with a distinct initial velocity are selected for detection by a microchannel plate detector. In combination with different delay times, variable laser intensities are used to simulate different impact velocities of ice grains onto the CDA's target (F.K. et al., manuscript in preparation). The detected signals are intensified by a preamplifier, visualized by a 12-bit digitizer card (Acqiris) and recorded using LabVIEW. Flow injection of the tested solutions is accomplished with an injection valve (model MX9925, Rheodyne). 500 single spectra are averaged to achieve the co-added spectra, as presented in Extended Data Figs. 7, 8. The chemicals (pro analysi) were purchased from Sigma Aldrich. All solutions were freshly prepared with doubly distilled H$_2$O in lockable 50-ml sample cups.

Data availability. All CDA data used for this analysis are archived on PDS-SBN (http://sbn.psi.edu/archive/cocda). The exact time stamps of each data point are listed in Extended Data Table 1.

31. Srama, R. et al. The Cassini cosmic dust analyzer. *Space Sci. Rev.* **114**, 465–518 (2004).
32. Hillier, J. K., McBride, N., Green, S. F., Kempf, S. & Srama, R. Modelling CDA mass spectra. *Planet. Space Sci.* **54**, 1007–1013 (2006).
33. Postberg, F. et al. Composition of jovian dust stream particles. *Icarus* **183**, 122–134 (2006).
34. Srama, R. et al. The cosmic dust analyzer onboard Cassini: ten years of discoveries. *CEAS Space Jour.* **2**, 3–16 (2011).
35. Fiege, K. et al. Calibration of relative sensitivity factors for impact ionization detectors with high-velocity silicate microparticles. *Icarus* **241**, 336–345 (2014).
36. Mocker, A. et al. A 2 MV Van de Graaff accelerator as a tool for planetary and impact physics research. *Rev. Sci. Instrum.* **82**, 095111 (2011).
37. Delcorte, A., Segda, B. G. & Bertrand, P. ToF-SIMS analyses of polystyrene and dibenzanthracene: evidence for fragmentation and metastable decay processes in molecular secondary ion emission. *Surf. Sci.* **381**, 18–32 (1997).
38. Stephan, T., Jessberger, E. K., Heidd, C. H. & Rost, D. TOF-SIMS analysis of polycyclic aromatic hydrocarbons in Allan Hills 84001. *Meteorit. Planet. Sci.* **38**, 109–116 (2003).
39. Wiederschein, F., Vöhringer-Martinez, E. & Postberg, F. Charge separation and isolation in strong water droplet impacts. *Phys. Chem. Chem. Phys.* **17**, 6858–6864 (2015).
40. Le Roy, L. et al. COSIMA calibration for the detection and characterization of the cometary solid organic matter. *Planet. Space Sci.* **105**, 1–25 (2015).
41. Waite, J. H. Jr et al. The Cassini ion and neutral mass spectrometer (INMS) investigation. *Space Sci. Rev.* **114**, 113–231 (2004).
42. Perry, M. E. et al. Cassini INMS measurements of Enceladus plume density. *Icarus* **257**, 139–162 (2015).
43. Kieffer, S. W. et al. A clathrate reservoir hypothesis for Enceladus' south polar plume. *Science* **314**, 1764–1766 (2006).
44. Ingersoll, A. P. & Pankine, A. A. Subsurface heat transfer on Enceladus: conditions under which melting occurs. *Icarus* **206**, 594–607 (2010).
45. Gaston, C. J. et al. Unique ocean-derived particles serve as a proxy for changes in ocean chemistry. *J. Geophys. Res.* **116**, D18310 (2011).
46. Keene, W. C. et al. Chemical and physical characteristics of nascent aerosols produced by bursting bubbles at a model air–sea interface. *J. Geophys. Res.* **112**, D21202 (2007).
47. Facchini, M. C. et al. Primary submicron marine aerosol dominated by insoluble organic colloids and aggregates. *Geophys. Res. Lett.* **35**, L17814 (2008).
48. Russell, L. M. et al. Carbohydrate-like composition of submicron atmospheric particles and their production from ocean bubble bursting. *Proc. Natl Acad. Sci. USA* **107**, 6652–6657 (2010).
49. Burrows, S. M. et al. A physically based framework for modeling the organic fractionation of sea spray aerosol from bubble film Langmuir equilibria. *Atmos. Chem. Phys.* **14**, 13601–13629 (2014).
50. Jayarathne, T. et al. Enrichment of saccharides and divalent cations in sea spray aerosol during two phytoplankton blooms. *Environ. Sci. Technol.* **50**, 11511–11520 (2016).
51. Schmitt-Kopplin, P. et al. Dissolved organic matter in sea spray: a transfer study from marine surface water to aerosols. *Biogeosciences* **9**, 1571–1582 (2012).
52. McCollom, T. M. et al. The influence of carbon source on abiotic organic synthesis and carbon isotope fractionation under hydrothermal conditions. *Geochim. Cosmochim. Acta* **74**, 2717–2740 (2010).
53. Milesi, V. et al. Thermodynamic constraints on the formation of condensed carbon from serpentinization fluids. *Geochim. Cosmochim. Acta* **189**, 391–403 (2016).
54. Williams, L. B. et al. Organic molecules formed in a "primordial womb". *Geology* **33**, 913–916 (2005).
55. Cody, G. D. et al. Establishing a molecular relationship between chondritic and cometary organic solids. *Proc. Natl Acad. Sci. USA* **108**, 19171–19176 (2011).
56. Stevenson, F. J. *Humus Chemistry: Genesis, Composition, Reactions* (Wiley-Interscience, New York, 1982).
57. Hänninen, K. I., Klöcking, R. & Helbig, B. Synthesis and characterization of humic acid-like polymers. *Sci. Total Environ.* **62**, 201–210 (1987).
58. Alexander, C. M. O'D. et al. The nature, origin and modification of insoluble organic matter in chondrites, the major source of Earth's C and N. *Chem. Erde* **77**, 227–256 (2017).
59. Alexander, C. M. O'D., Fogel, M., Yabuta, H. & Cody, G. D. The origin and evolution of chondrites recorded in the elemental and isotopic compositions of their macromolecular organic matter. *Geochim. Cosmochim. Acta* **71**, 4380–4403 (2007).
60. Derenne, S. & Robert, F. Model of molecular structure of the insoluble organic matter isolated from Murchison meteorite. *Meteorit. Planet. Sci.* **45**, 1461–1475 (2010).
61. Remusat, L. Organic material in meteorites and the link to the origin of life. *BIO Web Conf.* **2**, 03001 (2014).
62. Sephton, M. Organic compounds in carbonaceous meteorites. *Nat. Prod. Rep.* **19**, 292–311 (2002).
63. Pizzarello, S., Cooper, G. W. & Flynn, G. J. in *Meteorites and the Early Solar System II* (eds Lauretta D. & McSween H. Y.) 625–651 (Univ. of Arizona Press, Tucson, 2006).
64. Bardyn, A. et al. Carbon-rich dust in comet 67P/Churyumov–Gerasimenko measured by COSIMA/Rosetta. *Mon. Not. R. Astron. Soc.* **469**, S712–S722 (2017).
65. Altwegg, K. et al. Organics in comet 67p – a first comparative analysis of mass spectra from ROSINA–DFMS, COSAC and Ptolemy. *Mon. Not. R. Astron. Soc.* **469**, S130–S141 (2017).
66. Tissot, B. P. & Welte, D. H. *Petroleum Formation and Occurrence* 2nd edn (Springer, Berlin, 1984).
67. Didyk, B. M. & Simoneit, B. R. T. Hydrothermal oil of Guaymas Basin and implications for petroleum formation mechanisms. *Nature* **342**, 65–69 (1989).
68. McKinnon, W. B., Simonelli, D. P. & Schubert, G. in *Pluto and Charon* (eds Stern, S. A. & Tholen, D. J.) 295–343 (Univ. of Arizona Press, Tucson, 1997).
69. Sephton, M. A. et al. Hydropyrolysis: a new technique for the analysis of macromolecular material in meteorites. *Planet. Space Sci.* **53**, 1280–1286 (2005).
70. Kissel, J. & Krueger, F. R. The organic component in dust from comet Halley as measured by the PUMA mass spectrometer on board Vega 1. *Nature* **326**, 755–760 (1987).
71. Schoell, M. Multiple origins of methane in the Earth. *Chem. Geol.* **71**, 1–10 (1988).
72. Von Damm, K. L. et al. The Escanaba Trough, Gorda Ridge hydrothermal system: temporal stability and subseafloor complexity. *Geochim. Cosmochim. Acta* **69**, 4971–4984 (2005).
73. Horányi, M., Juhász, A. & Morfill, G. E. Large-scale structure of Saturn's E-ring. *Geophys. Res. Lett.* **35**, L04203 (2008).
74. Hsu, H.-W. et al. Understanding the E-ring puzzle. *AGU Fall General Assembly*, abstr. P33E-01 (2016).
75. Waite, J. H. et al. The process of tholin formation in Titan's upper atmosphere. *Science* **316**, 870–875 (2007).
76. Lavvas, P. et al. Aerosol growth in Titan's ionosphere. *Proc. Natl Acad. Sci. USA* **110**, 2729–2734 (2013).
77. Charvat, A. & Abel, B. How to make big molecules fly out of liquid water: applications, features and physics of laser assisted liquid phase dispersion mass spectrometry. *Phys. Chem. Chem. Phys.* **9**, 3335–3360 (2007).
78. Srama, R. *Cassini–Huygens and Beyond—Tools for Dust Astronomy*. Habil. Thesis, Univ. of Stuttgart (2009).

a)

b)
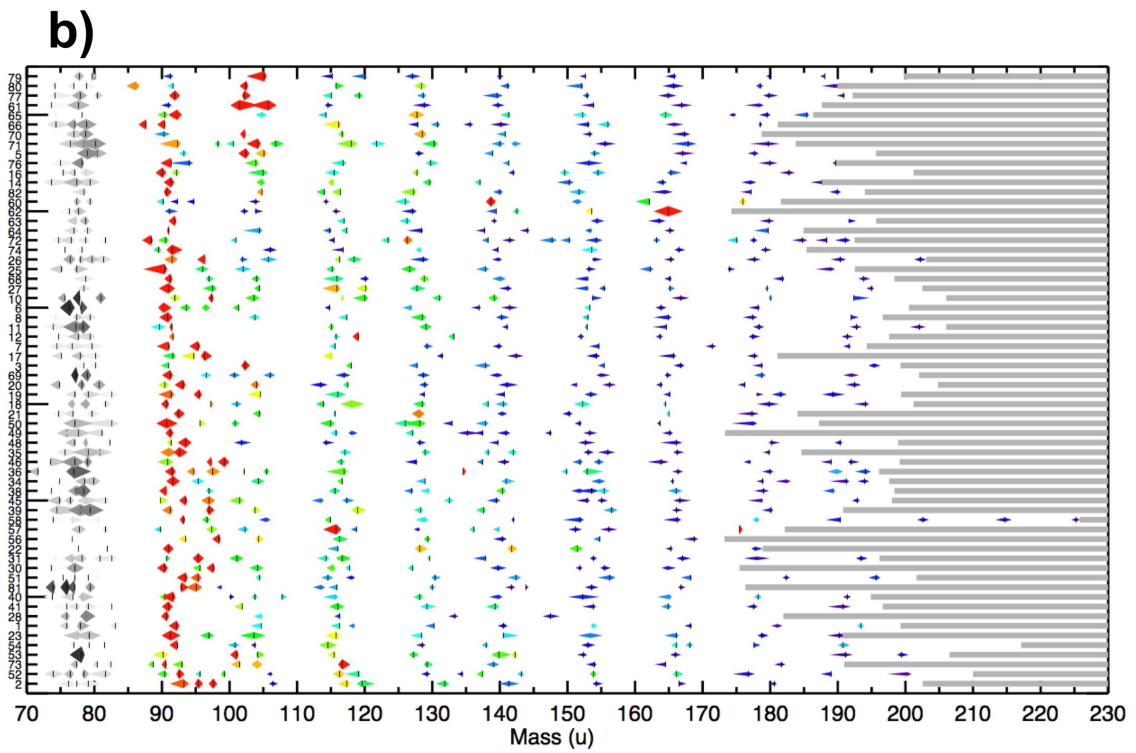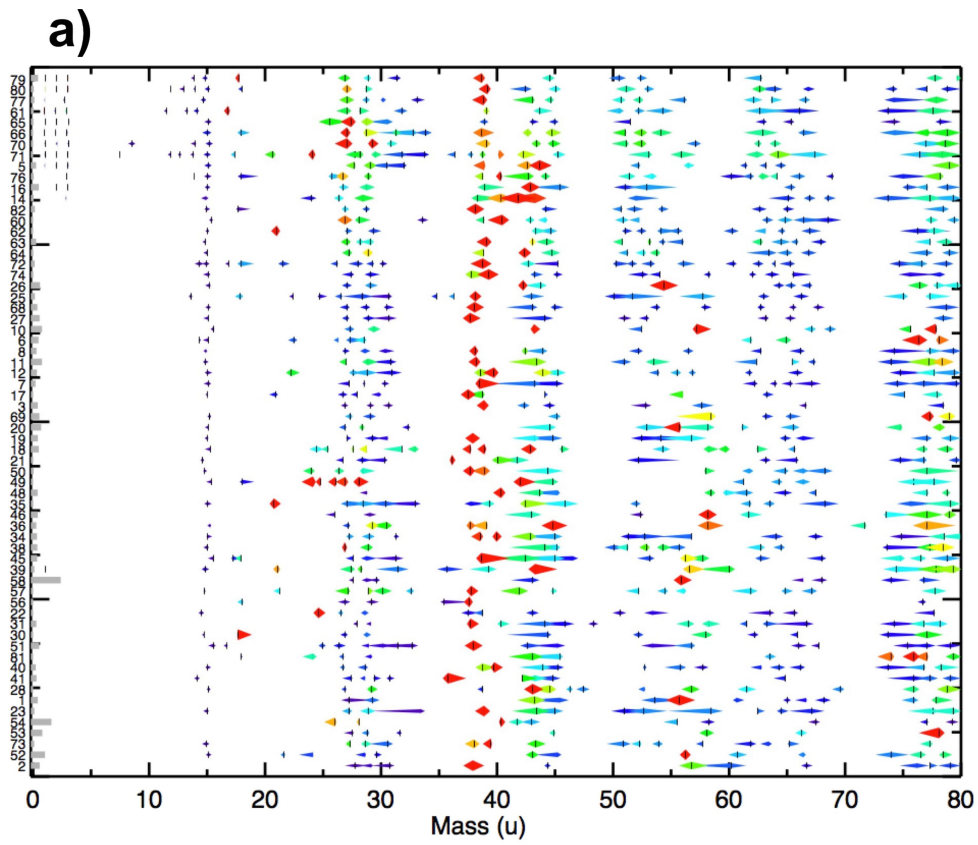
Extended Data Fig. 1 | See next page for caption.

Extended Data Fig. 1 | Semi-quantitative display of CDA HMOC spectra. a, **b**, Identified organic mass lines of individual HMOC spectra. The distribution of resolved mass lines and flank peaks of 64 HMOC spectra with the most distinct HMOCs are shown (see Methods, 'Selection of 64 high-quality spectra for Fig. 1 and Extended Data Figs. 1 and 3'). 19 more spectra with a high level of interference with water-cluster ions or low signal-to-noise ratio are not included here (see Extended Data Table 1). All peaks depicted here are also part of the data shown in Fig. 1b. The spectrum number (as defined in Extended Data Table 1) is indicated on the left as an identifier of the event. The extent is indicated by the horizontal length and the relative normalized amplitude of each spectral feature is given by the length in the vertical direction and the colour code (red being the highest and blue the lowest amplitude). The largest horizontal span of the symbol marks the peak maximum. In **b**, the amplitudes between 70 u and 85 u shown in grey indicate that they are not to scale with the symbols shown at higher masses (they would be much larger; see Fig. 1b for comparison). Spectra are sorted by their impact speed, as estimated from the orbital elements of the impacting grain, with the highest speed (~15 km s^{-1}) at the top of the graphs and the lowest (~5 km s^{-1}) at the bottom. Because the exact orbital elements are unknown, each impact speed has substantial intrinsic uncertainties, given in Extended Data Table 1. The 12 spectra for which a minimum impact speed could be derived from the presence of hydrogen mass lines (Extended Data Table 1; see Methods, 'Selection of 64 high-quality spectra for Fig. 1 and Extended Data Figs. 1 and 3') are placed at the top. The highest mass at which the recording of the CDA TOF spectrum ends varies between 174 u and 226 u (Methods, 'Short description of CDA's chemical analyser subsystem'), as indicated by the grey horizontal bars. As a consequence, the frequency of the HMOC peaks around 178 u and 191 u in Fig. 1b is reduced because not all individual spectra cover this mass range. The absolute masses in each individual spectrum have an intrinsic uncertainty (absolute value) of ±1 u at 80 u and ±2 u at 180 u owing to the limited calibration accuracy of the CDA in this high-mass regime. The mass intervals between peaks, however, are accurate to the integer level.
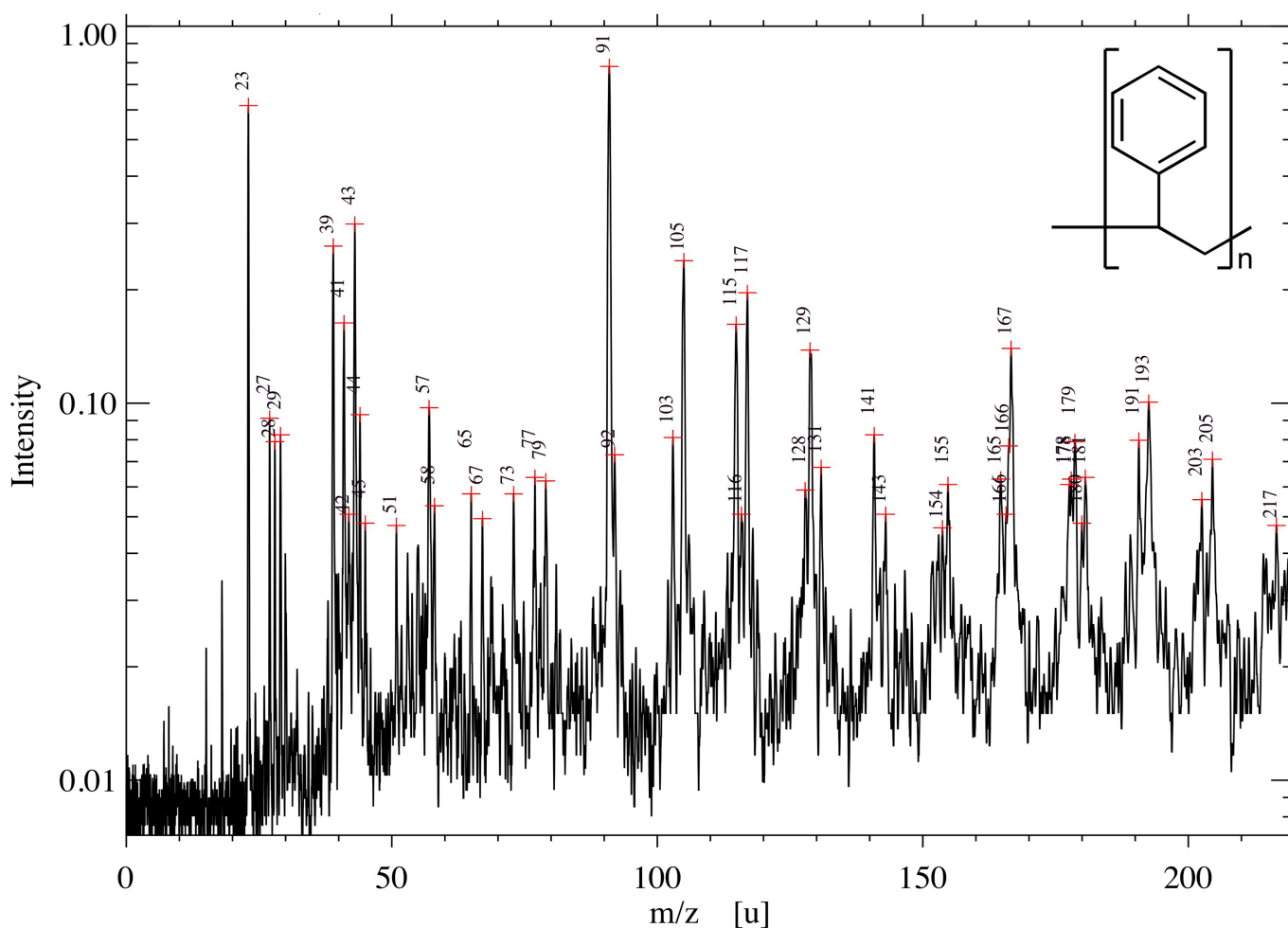
Extended Data Fig. 2 | Impact ionization laboratory spectrum of a polystyrene bead. The figure was modified from figure 5 of ref. [19]. The x-axis shows m (mass) over z (cation charge), with $z = 1$ for all major species. The impact ionization TOF mass spectrum of a polystyrene particle with a radius of ~1 μm was recorded at the Heidelberg dust accelerator facility[36] with an impact speed of 5.2 km s^{-1}. Above 100 u and below 70 u the spectrum shows cationic fragments, in good agreement with the CDA HMOC spectra and their characteristic spacing of 12.5 u. The inset shows the molecular structure of the polymer. See the main text and Methods section 'Inferring the origin of HMOC peaks in CDA spectra' for further discussion.
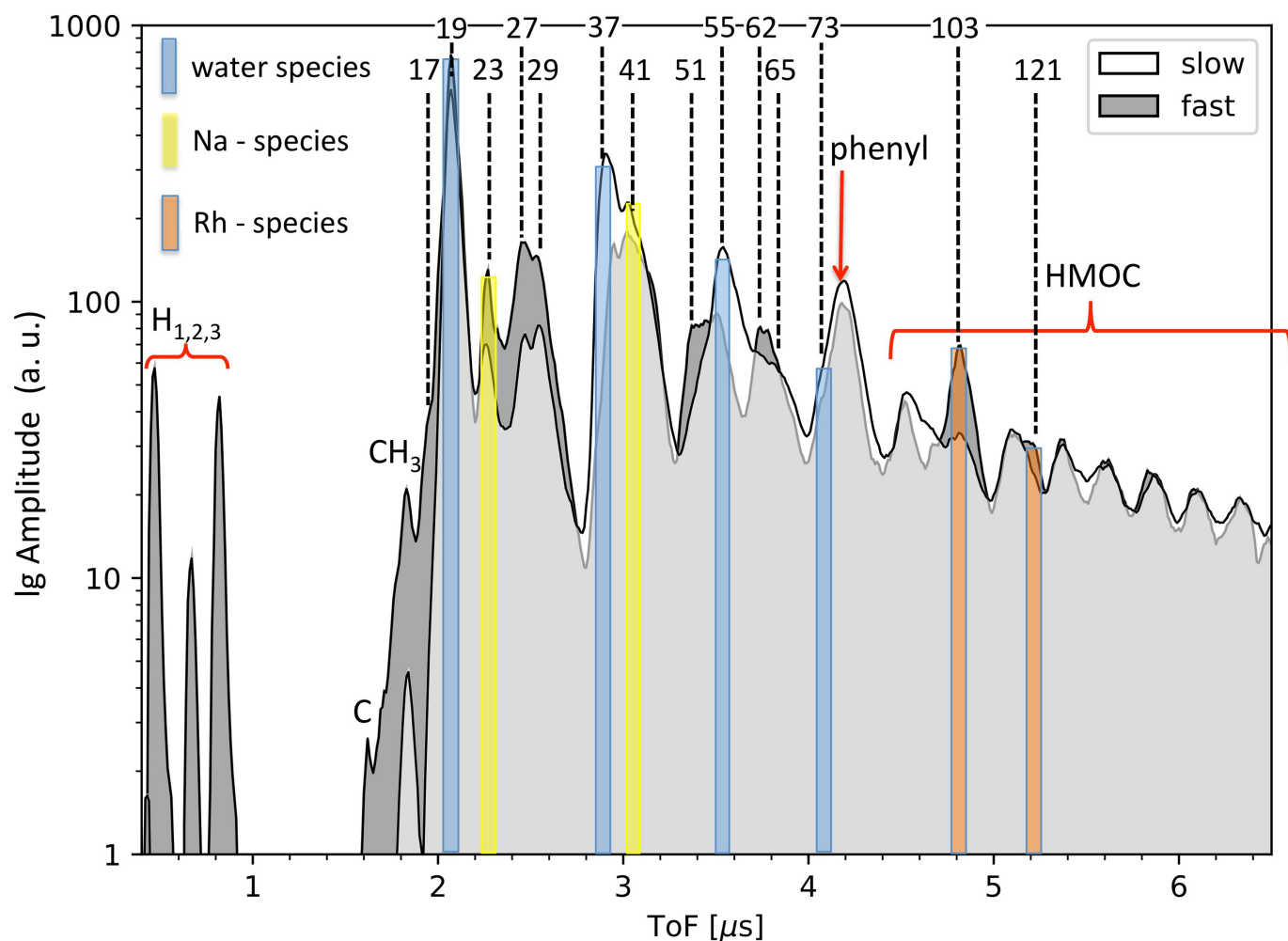
Extended Data Fig. 3 | Comparison of CDA HMOC spectra from fast and slow impacts. White and grey spectra represent the average of all spectra from impacts below and above ~10 km s^{-1}, respectively (see Methods, 'Selection of 64 high-quality spectra for Fig. 1 and Extended Data Figs. 1 and 3'). All signatures with possible major contributions from inorganic species are colour-shaded as in Fig. 1. Signatures not marked are exclusively or mostly due to organic cations. The abundance and position of the HMOC species is relatively independent of the impact speed of the ice grain (see also Extended Data Fig. 1). By contrast, fast impacts induce stronger organic fragmentation signatures at masses below 70 u and HMOCs form more distinct, evenly spaced groups, characteristic of impact-induced dissociation processes. In turn, slow impacts show more abundant intact benzene-like cations. There seems to be a tendency of some organic cations to carry fewer H atoms at fast impacts (27 u, 51 u and 62 u), which is indicative of 'softer' ionization from the slower impact. In fast spectra, interference with water-cluster ions is less frequent than at lower speeds. In contrast to fast spectra, fragmentation below CH_3^+ (15 u) is usually not observed in slow spectra. Spectra from slow impacts are prone to abundant water clustering, creating mass lines of the form $H^+(H_2O)_n$, with $n = 1-4$, at 19 u, 37 u, 55 u and 73 u (blue). In fast spectra, clustering is limited and only the mass lines at 19 u and 37 u are generally present; occasionally, formation of the smaller water ions OH^+ (17 u) and H_2O^+ (18 u) is observed. Similarly, Rh^+ (103 u) forms from excavation of the impact target only at fast impacts and interferes with HMOC species there. To a lesser extent, this is also true for the rhodium–water cluster $Rh^+(H_2O)$ at 121 u. See the individual CDA spectra in Extended Data Fig. 4 for comparison. a.u., arbitrary units; ToF, time of flight; lg, log.

a)

2008−131/02:18:03 (1589079331)

b)

2005−358/15:57:10 (1514132787)
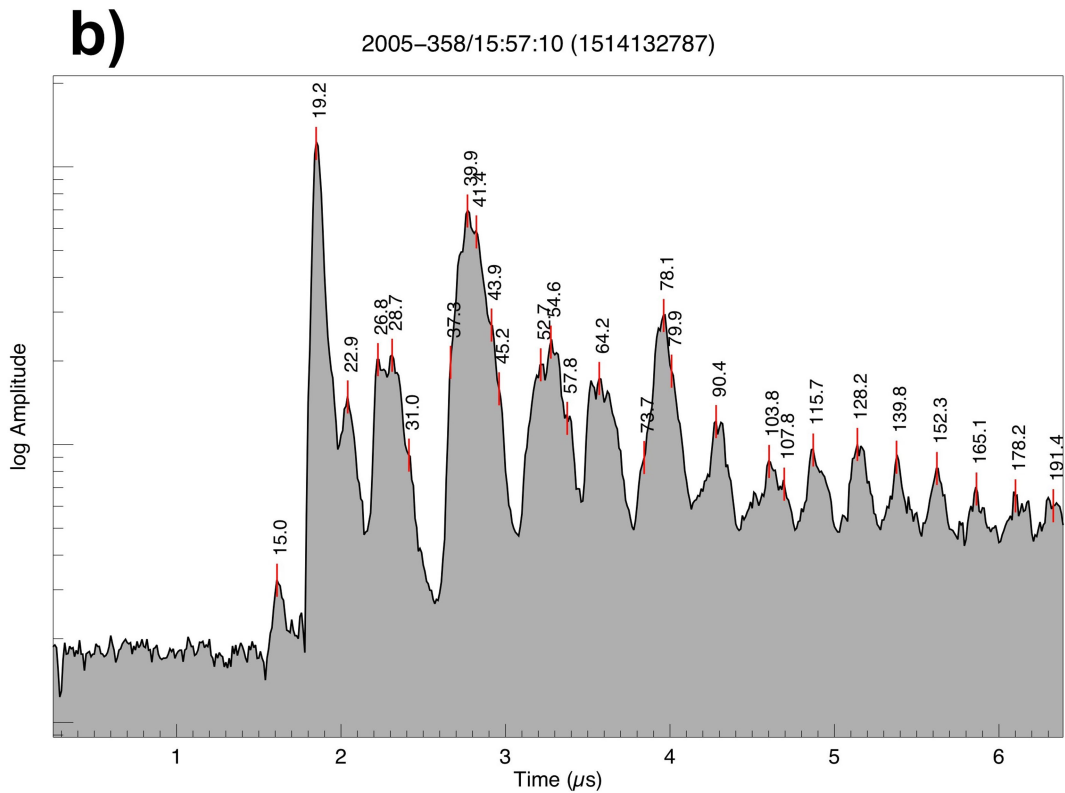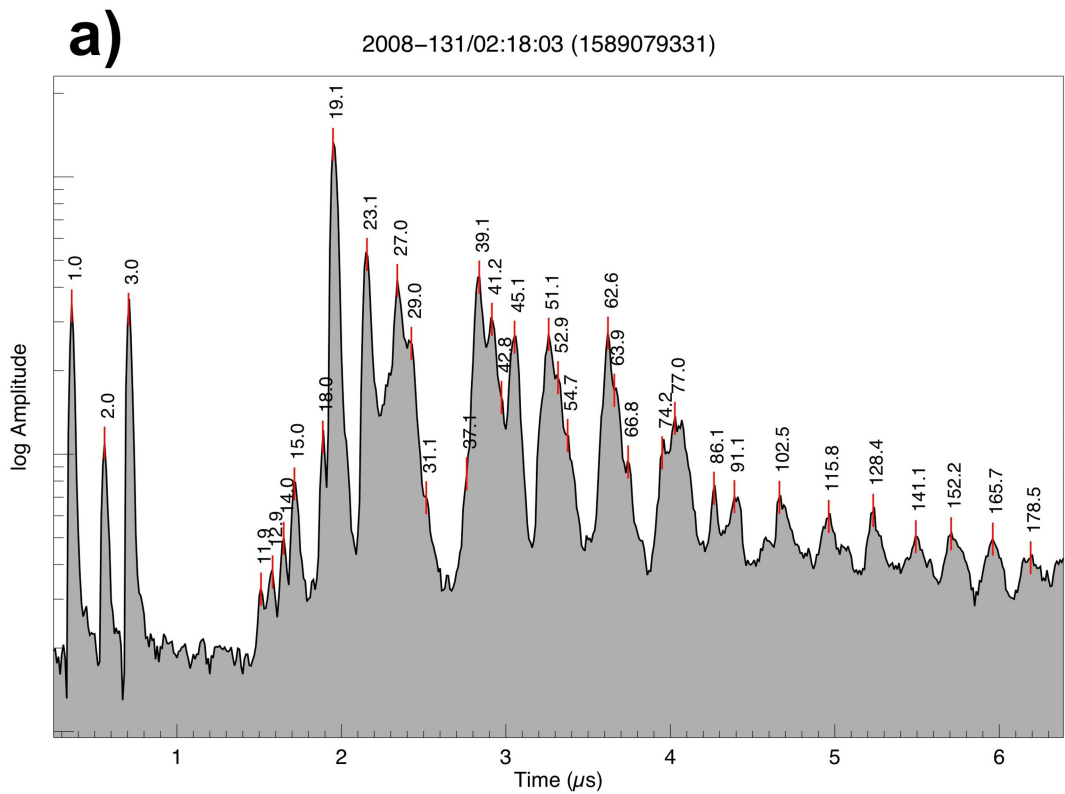
Extended Data Fig. 4 | See next page for caption.

Extended Data Fig. 4 | Example CDA spectra from individual HMOC-type ice grains. In these individual spectra, the peak definition is naturally higher than in the co-added spectra shown in Fig. 1 and Extended Data Fig. 3, and therefore some of the spectral features collected in Fig. 1b become more apparent. **a**, HMOC spectrum from one of the fastest recorded impacts (12–18 km s^{-1}). The appearance of hydrogen cations (H$^+$, H$_2^+$ and H$_3^+$) at 1 u, 2 u and 3 u, as well as the disintegration of the CH$_3^+$ ion into CH$_2^+$, CH$^+$ and C$^+$ (12 u–15 u) and the formation of H$_2$O$^+$ (18 u), are evidence of the high-speed impact. The abundance of unsaturated small cations below 70 u, probably fragments from aromatic structures, is increased compared to slower spectra. The frequently occurring mass line at 45 u (Fig. 1b and Extended Data Fig. 1) is noticeable; it cannot originate from pure hydrocarbons and requires heteroatoms, probably oxygen in this case. While a 45 u feature is quite common in our HMOC dataset, the peak at 86 u is only apparent in this spectrum. **b**, HMOC spectrum from a grain detected at intermediate speed (5–8 km s^{-1}). High-mass fragments and benzene species are abundant whereas further fragmentation of the benzene ring into C$_5$ and C$_4$ species is less apparent compared to high-velocity impacts (**a**). We note that organic cations with 2, 3, 4 and 5 C atoms show a tendency to carry more H atoms compared with the high-speed impact, which is indicative of 'softer' ionization from the slower impact. Organic fragmentation below CH$_3^+$ is usually not observed in this speed regime.

a)

2006-337/00:41:01 (1543799608)

Regular mass range
(high resolution)

Extended mass range
(low resolution)

artefact

≈ 800 - 1250 u

≈ 250 - 500 u

≈ 1500 - 2100 u

lg Amplitude (a. u.)

1.0   6.4   40

Time of Flight (µs)

b)

Total number of spectra: 83

Count

15

10

5

200   300   400   600   1000   1500

Mass (u)
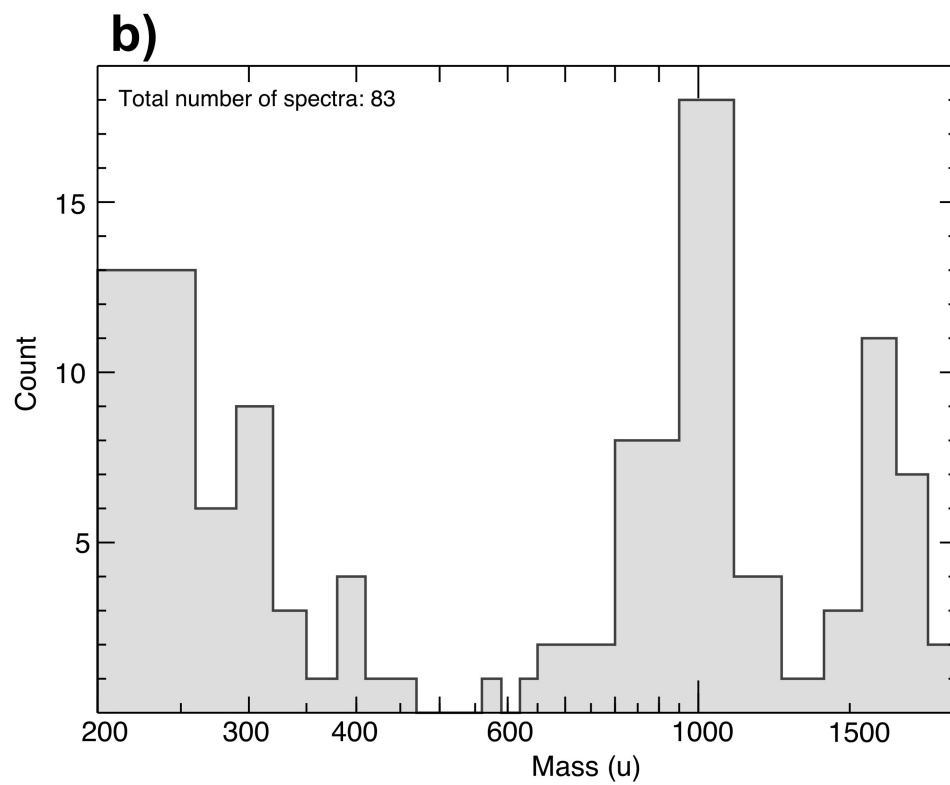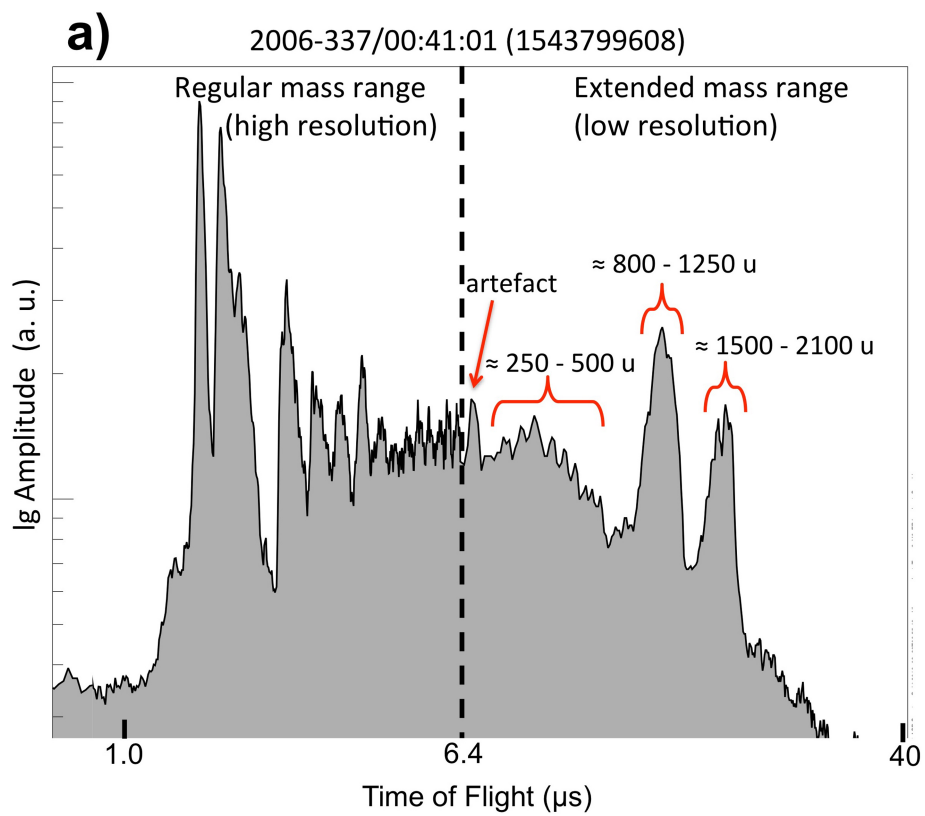
Extended Data Fig. 5 | See next page for caption.

Extended Data Fig. 5 | Example HMOC CDA mass spectrum with extended mass range and statistics for all features. a, Ice grain spectrum showing the HMOC event with the strongest extended mass range signal of the dataset. The dashed line at 6.4 μs divides the spectrum into the high-resolution part (10 ns sampling) and the low-resolution part (100 ns sampling) (see Methods, 'Short description of CDA's chemical analyser subsystem'). There are several relatively narrow peaks between 250 u and 500 u and two much more extended features peaking at about 1,000 u and 1,800 u. In this case, the cations with mass in excess of 200 u are more than twice as abundant (defined by the area under the curve) as those below 200 u. We note the logarithmically scaled TOF axis in this case. These features are usually less frequent and less pronounced than in the extreme case shown here. The extended spectrum frequently shows an instrument-artefact peak at 6.8 μs, which was not considered in our analysis. **b**, Histogram showing the frequency of occurrences of the features observed in the extended mass range. The definition, and thus significance, of peaks in the extended spectrum is generally lower than in the nominal spectrum. In particular, features above 500 u are sometimes ambiguous and their interpretation should be taken with great caution. However, the statistics shows three preferred mass regions: 200 u–500 u with decreasing frequency, around 1,000 u and around 1,700 u. Even if no sizeable peaks are present, the cation signal in the HMOC spectra is generally higher than the noise level when the low-resolution recording starts and typically only decays to noise level at around 500 u or later.

2012–087/18:30:38 (1711567323)
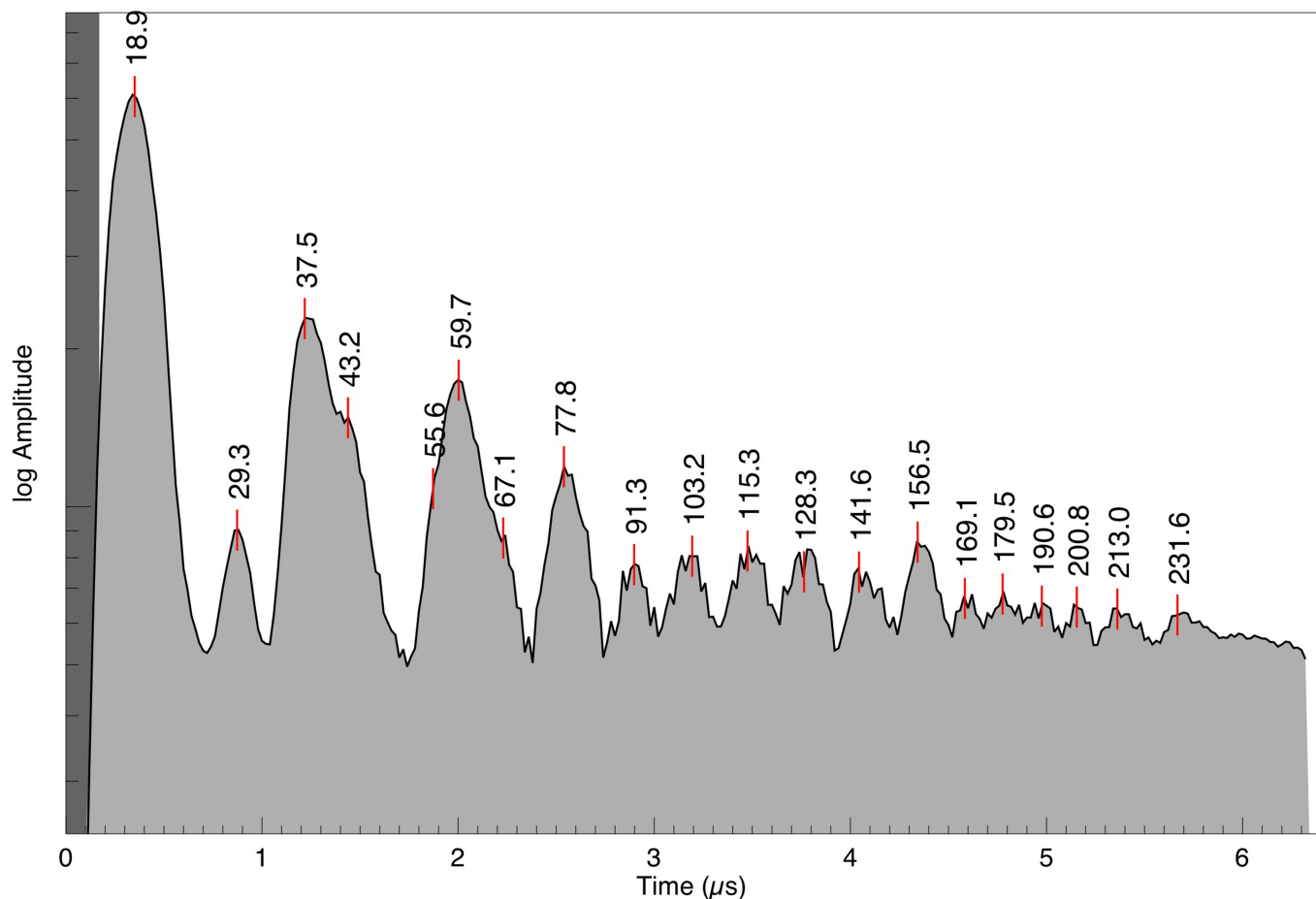
Extended Data Fig. 6 | CDA HMOC spectrum recorded in the Enceladean plume. During Cassini's E17 flyby of Enceladus' south pole at 75 km altitude, where the CDA recorded about 40 plume spectra with its full mass range, one spectrum was of the HMOC type. This is in agreement with the proportion of this particle type being a few per cent in the plume and in the E ring close to Enceladus (see Methods, 'Relative frequency of HMOC-type grains depends on impact speed and distance to Enceladus orbit.'). The flyby speed determined the impact speed of 8.6 km s^{-1} and the particle had a radius of about 2 μm. To operate the CDA in the dense dust environment of the plume, the instrument settings had to be modified in a way that compromised the spectrum quality (lower sensitivity and lower mass resolution; see Extended Data Fig. 4 for comparison). The spectrum is baseline-corrected. On the only occasion when the CDA recorded a large number of spectra with high cadence directly in the plume during Cassini's E5 flyby[9], the spectral range was truncated below about 100 u to allow for a higher data rate. This unfortunately did not allow the identification of the defining HMOC signatures.
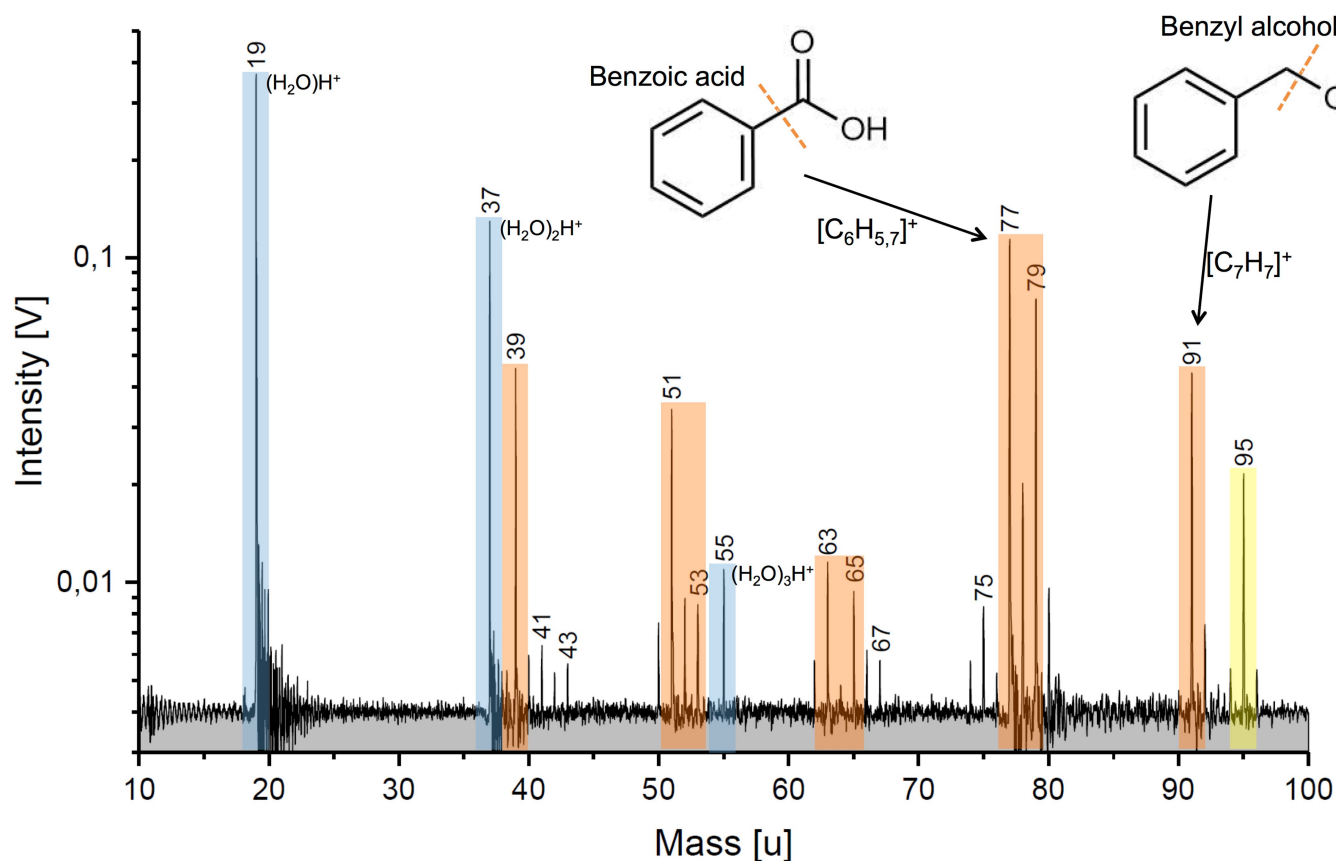
Extended Data Fig. 7 | Laser ionization mass spectrum of benzoic acid and benzyl alcohol dissolved in water. Analogue TOF mass spectrum recorded with the liquid microbeam ionization setup (see Methods, 'Laser dispersion analogue experiments for icy dust impacts' and Extended Data Fig. 9) to simulate the formation of tropylium and benzene cations and their fragmentation ions at impact speeds[78] of the order of 10 km s^{−1}. The concentrations of benzoic acid and benzyl alcohol are 3 g l^{−1} and 0.2 g l^{−1}, respectively. Water ions are marked in blue, aromatic ions and ions from aromatic fragmentation are marked in orange and mixed organic–water species are yellow. To yield both benzene cations (77 u–79 u) and tropylium ions (91 u), two different aromatic structures are required (Fig. 2). The predominant aromatic fragments of benzoic acid are at 77 u and 79 u, whereas benzyl alcohol almost exclusively forms tropylium ions at 91 u. The peak at 95 u is a water cluster of the phenyl cation, which is much more pronounced than in the HMOC spectra. Although the strong phenyl–water cluster signature here illustrates the intimate mixing of organics with water, the much lower 95 u signature in HMOC spectra argues for less efficient mixing of organics with water there, probably due to a core–shell structure that physically separates organics from ice in the grain. Cations from the fragmented ring can be seen at 39 u, 51 u–53 u and 63 u–65 u and agree with the CDA observations (Fig. 1b). In contrast to the CDA spectra, however, saturated C_3 fragments (41 u–43 u) are depleted, and C_2 (27 u–29 u) and C_1 (15 u) fragment cations are entirely absent, confirming the presence of an abundance of aliphatic cations in HMOC grains. The ratios of benzene and tropylium ions and the water ions match the HMOC spectra well. The total concentration of organic species used here (~0.32% by weight) can be used to estimate a lower limit for the concentration of organics in CDA HMOC grains for two reasons. First, in the analogue experiment we selected substances that most efficiently yield the desired aromatic species and other, less efficient precursors would yield even lower signals at 77 u and 91 u. Second, to account for both the low- and high-mass fragments between 100 and 2,000 u, which are absent in the laboratory spectrum, additional organic substances or larger molecules would be needed to further increase the organic concentration. Therefore, the concentration in Enceladean HMOC ice grains in many cases can be estimated to be near or even above the per cent level.
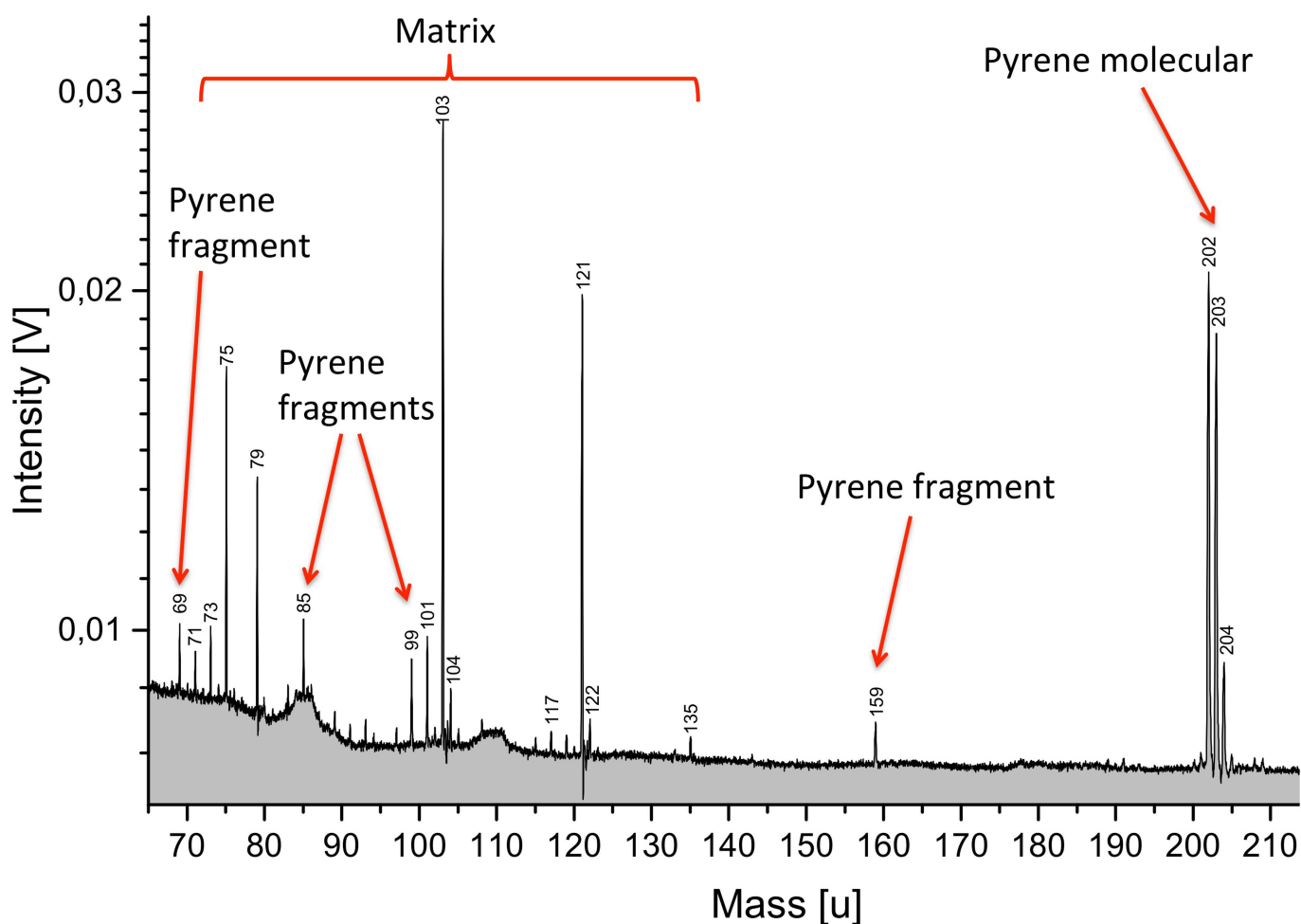
Extended Data Fig. 8 | Laser ionization analogue spectrum of pyrene in water–acetic acid mixture. Cationic TOF mass spectrum recorded with the liquid microbeam ionization setup (see Methods, 'Laser dispersion analogue experiments for icy dust impacts', and Extended Data Fig. 9) containing 0.1% pyrene dissolved in a mixture of water and acetic acid. The laser pulse simulates an ice grain impact with a speed[78] of about 10 km s^{-1}. Features marked as 'pyrene fragment' do not appear in the blank experiment with just the solvent mixture and are either direct pyrene fragments or cations formed from pyrene fragments clustering with the solvent (for example, at 159 u). The molecular mass lines of pyrene are about 10 times more abundant than those of any fragments, indicating the stability of the PAH molecule. In contrast to CDA HMOC spectra, no isolated benzene ring fragment (77 u or 91 u) forms.
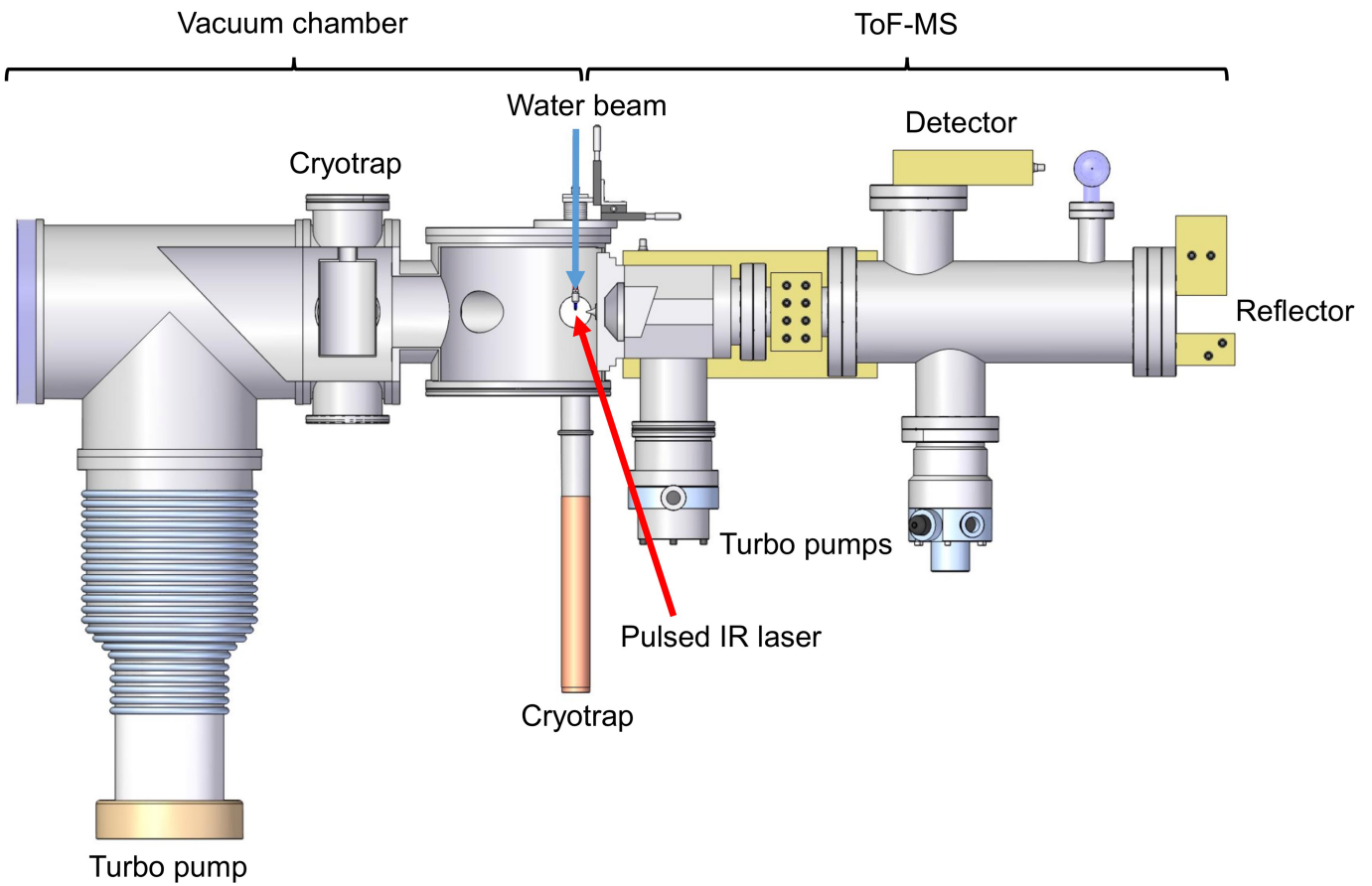
Extended Data Fig. 9 | Laboratory setup used to simulate ice grain impacts onto space-borne impact ionization detectors. See Methods, 'Laser dispersion analogue experiments for icy dust impacts', for a detailed description of the setup.

E14, E17, E18 Ice Grain Spectrum
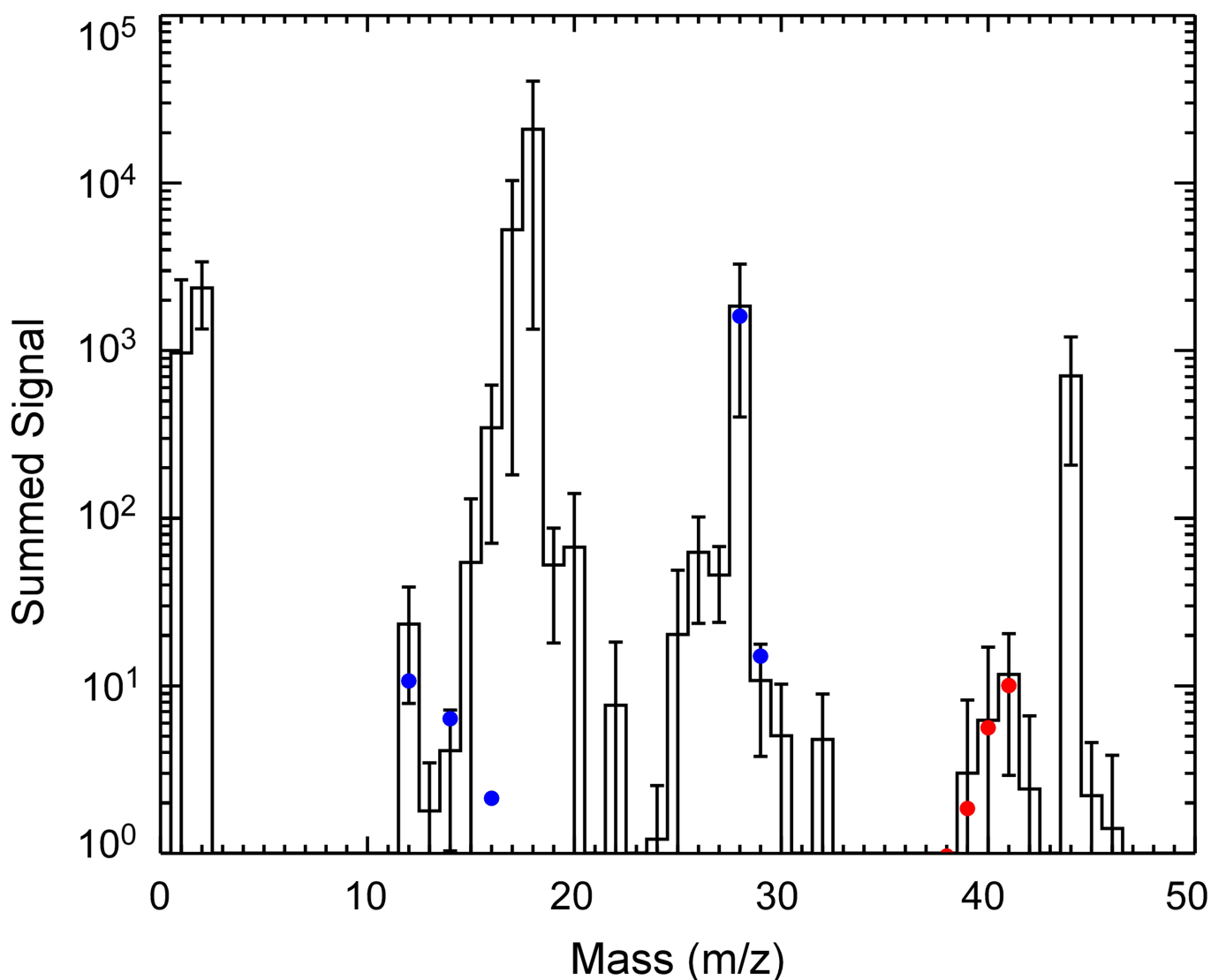
Extended Data Fig. 10 | Co-added INMS ice grain spike spectrum from three plume encounters. See Methods section 'INMS ice grain spectrum' for details on how the spectrum was composed and analysed. Error bars (1 s.d.) are derived from the dispersion of the count rate from the three separate measurements of the individual encounters. The spectrum suggests the presence of CO fragments (blue circles) as an oxygen-bearing species. N_2 has very low abundance and contributes less than ~10% of the 28 u signal. CO_2 and C_2H_4 collectively contribute less than ~10% of the 28 u signal. CO (blue circles) is required to fit the rest of the 28 u signal and the entire 29 u signal and matches its other dissociative peaks (C at 12 u and CO^{++} at 14 u) well. The spectrum also indicates the presence of nitrogen-bearing species: the 'stair step' pattern around 41 u matches best to the C_2H_3N spectrum (red circles).
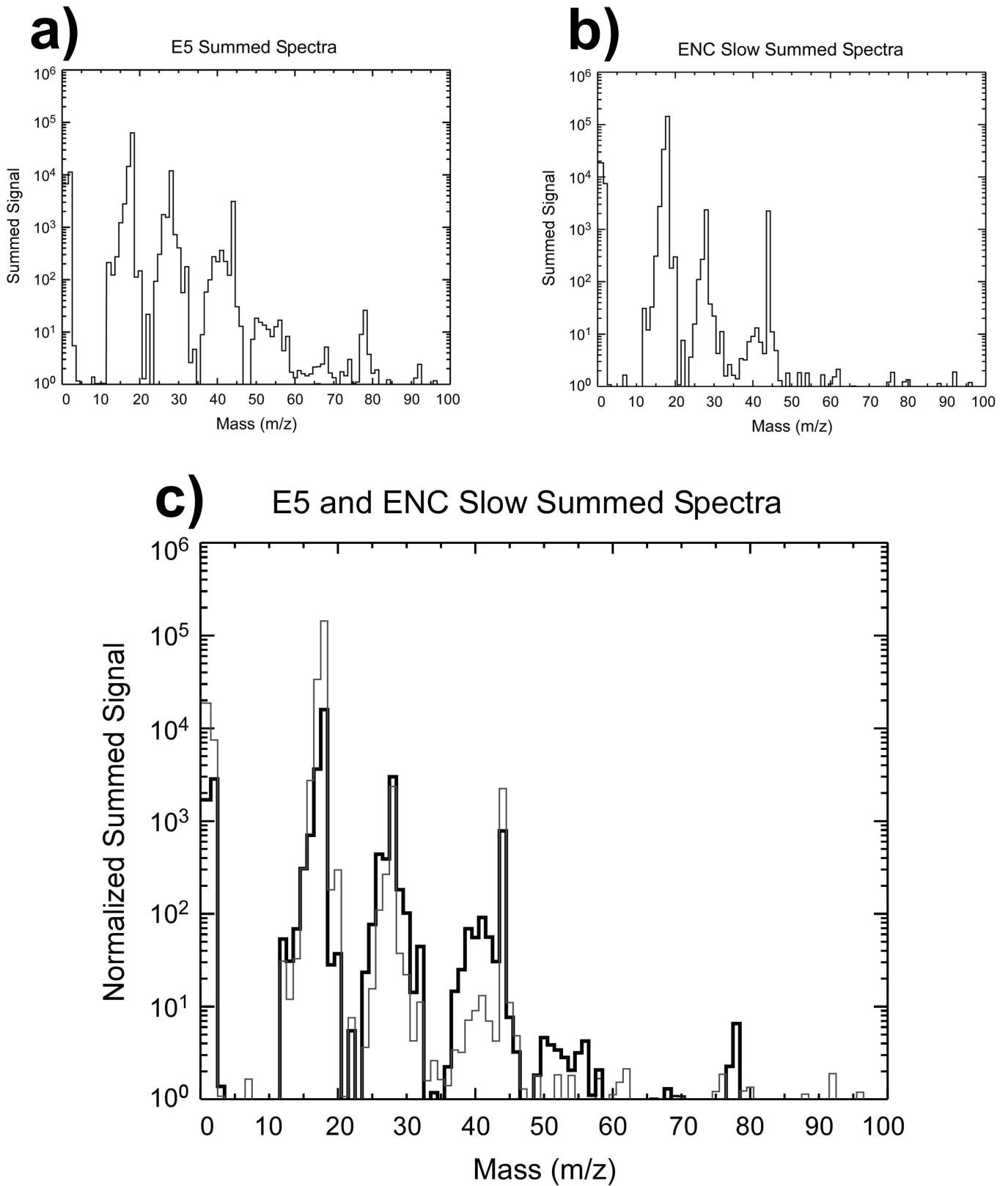
Extended Data Fig. 11 | INMS spectra used to produce the differenced spectrum in Fig. 3. a, **b**, The individual spectra for fast (E5; **a**) and slow (**b**) flybys are shown. **c**, The spectra of **a** and **b** are plotted with the E5 (black) spectrum, which is normalized to match the 15 u signal of the slow spectrum (grey). The residual (difference) between the two spectra is plotted in Fig. 3.

a) Water-filled vent in the icy crust

b) Formation of ice coated organic particles
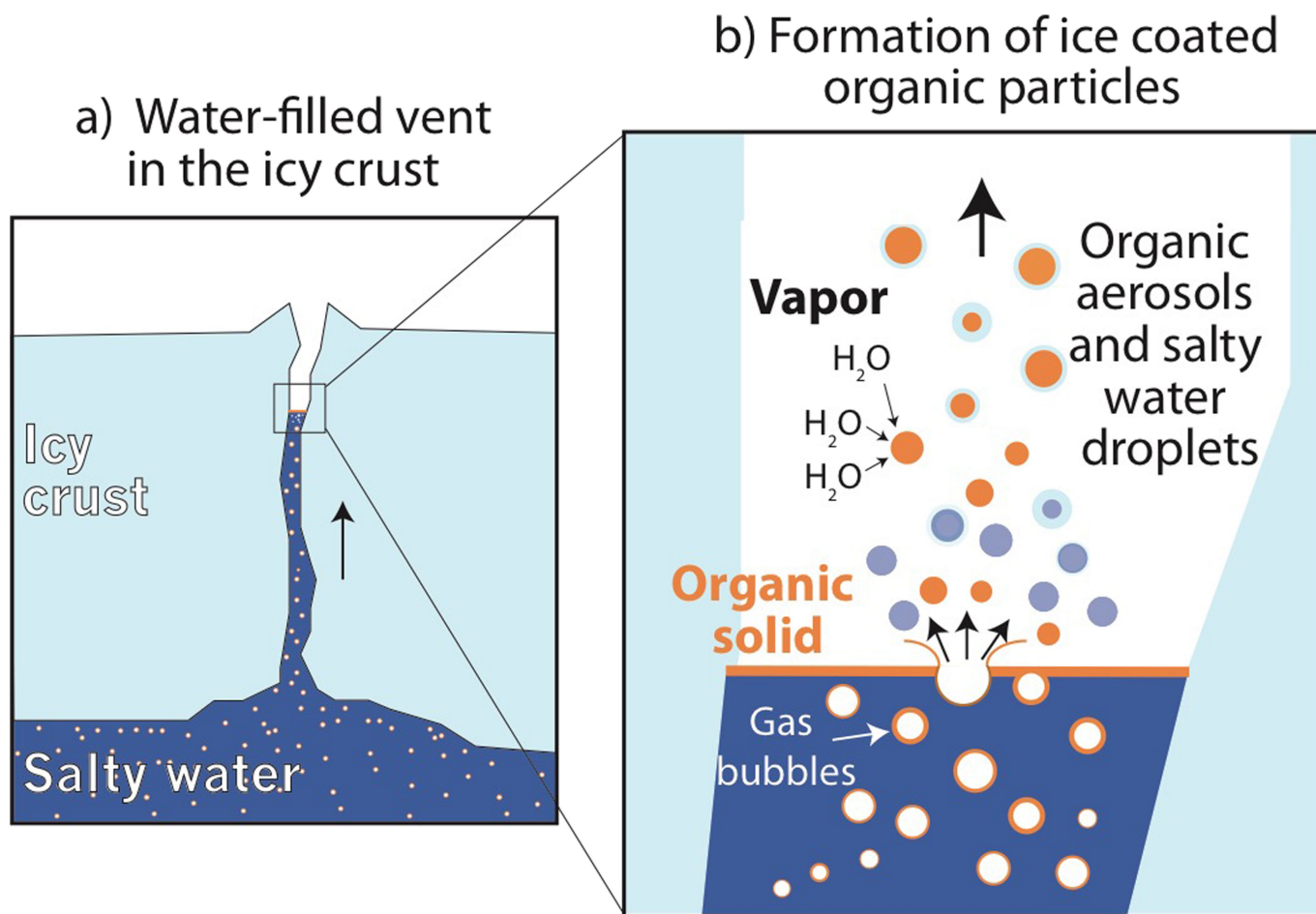
Extended Data Fig. 12 | Schematic on the formation of organic condensation cores from a refractory organic film. a, Ascending gas bubbles in the ocean[25] efficiently transport organic material[30] into water-filled cracks in the south polar ice crust. **b**, Organics ultimately concentrate in a thin organic layer (orange) on top of the water table, located inside the icy vents. When gas bubbles burst, they form aerosols made of insoluble organic material that later serve as efficient condensation cores for the production of an icy crust from water vapour, thereby forming HMOC-type particles. In parallel, larger, pure salt-water droplets form (blue), which freeze and are later detected by the CDA as salt-rich type-3 ice particles in the plume[8,9].

Extended Data Table 1 | List of 83 CDA mass spectra identified as of HMOC type

#	UTC	SCLK	QI (C)	R (R_S)	Z (R_S)	V_imp	V_-σ	V_+σ	Radius (μm)		
1	**2004-302/21:31:38**	1477691821	1.34E-14	8.6	-0.22	6.4	4.7	8.0	0.8	0.3	2
2	**2005-068/12:11:47**	1489063103	4.04E-14	3.53	0.01	5.0	3.7	6.3	1.2	0.5	3.2
3	**2005-068/19:12:50**	1489088367	2.30E-14	6.24	0.02	8.4	6.2	10.6	0.6	0.2	1.5
4	2005-068/19:57:18	1489091035	5.29E-14	6.61	0.02	8.4	6.2	10.6	0.7	0.3	1.7
5	**2005-177/09:15:19**	1498470176	1.02E-13	5.68	-1.44	8.6*	6.4	10.9	0.7	0.3	1.9
6	**2005-177/09:16:46**	1498470263	4.43E-14	5.67	-1.44	8.6	6.4	10.9	0.6	0.3	1.6
7	**2005-177/10:14:42**	1498473739	1.68E-13	5.21	-1.13	8.7	6.4	11.0	0.7	0.3	2
8	**2005-177/10:15:39**	1498473796	2.55E-14	5.2	-1.13	8.7	6.4	11.0	0.6	0.2	1.5
9	**2005-177/10:19:23**	1498474020	1.32E-14	5.18	-1.11	8.7	6.4	11.0	0.5	0.2	1.4
10	**2005-177/10:23:56**	1498474293	1.62E-14	5.14	-1.08	8.7	6.4	11.0	0.5	0.2	1.4
11	**2005-177/11:24:38**	1498477935	2.12E-14	4.69	-0.74	8.6	6.4	10.9	0.6	0.2	1.5
12	**2005-177/11:36:22**	1498478639	2.88E-14	4.61	-0.67	8.6	6.4	10.9	0.6	0.2	1.5
13	**2005-177/11:46:21**	1498479238	1.40E-14	4.54	-0.62	8.6	6.4	10.9	0.5	0.2	1.4
14	**2005-177/12:00:40**	1498480097	5.02E-14	4.45	-0.53	8.6*	6.3	10.8	0.6	0.3	1.7
15	2005-177/12:22:55	1498481432	5.43E-14	4.3	-0.4	8.5*	6.3	10.7	0.6	0.3	1.7
16	**2005-177/12:24:48**	1498481545	2.54E-14	4.29	-0.39	8.5*	6.3	10.7	0.6	0.2	1.5
17	**2005-177/12:31:51**	1498481968	3.26E-14	4.25	-0.35	8.5	6.3	10.7	0.6	0.3	1.6
18	**2005-177/12:48:40**	1498482977	1.10E-14	4.15	-0.25	8.4	6.2	10.6	0.5	0.2	1.4
19	**2005-177/12:49:08**	1498483005	4.12E-14	4.15	-0.24	8.4	6.2	10.6	0.6	0.3	1.7
20	**2005-177/12:50:33**	1498483090	1.82E-14	4.14	-0.24	8.4	6.2	10.6	0.6	0.2	1.5
21	**2005-177/12:56:32**	1498483449	5.27E-14	4.11	-0.2	8.3	6.2	10.5	0.7	0.3	1.8
22	**2005-177/15:48:06**	1498493743	2.20E-14	3.61	0.81	6.9	5.1	8.7	0.7	0.3	1.9
23	**2005-177/16:47:37**	1498497314	3.55E-13	3.69	1.11	6.6	4.9	8.3	1.2	0.5	3.1
24	2005-267/03:21:33	1506224999	3.40E-14	5.24	0.01	9.1	6.8	11.5	0.6	0.2	1.5
25	2005-267/03:22:22	1506225048	9.24E-14	5.25	0.01	9.2	6.8	11.5	0.6	0.3	1.7
26	2005-267/03:35:30	1506225836	2.75E-14	5.37	0.01	9.2	6.8	11.6	0.5	0.2	1.4
27	2005-267/07:34:31	1506240177	2.94E-14	7.52	0	8.8	6.5	11.2	0.6	0.2	1.5
28	2005-303/04:28:34	1509339440	3.74E-14	5.76	0.04	6.4	4.8	8.1	0.9	0.4	2.3
29	2005-303/04:43:14	1509340320	1.75E-14	5.85	0.04	6.5	4.8	8.2	0.8	0.3	2
30	**2005-303/04:48:04**	1509340610	4.42E-14	5.88	0.04	6.6	4.8	8.3	0.9	0.4	2.3
31	2005-303/05:03:27	1509341533	4.64E-14	5.98	0.04	6.6	4.9	8.4	0.9	0.4	2.3
32	2005-303/05:43:23	1509343929	4.32E-14	6.24	0.04	6.8	5.0	8.6	0.8	0.3	2.2
33	2005-303/05:53:09	1509344515	5.82E-13	6.3	0.04	6.8	5.1	8.6	1.2	0.5	3.2
34	2005-303/05:59:07	1509344873	7.83E-14	6.34	0.04	6.9	5.1	8.7	0.9	0.4	2.4
35	**2005-303/06:36:17**	1509347103	3.31E-13	6.59	0.04	7.0	5.2	8.8	1.1	0.4	2.9
36	**2005-303/06:41:04**	1509347390	8.31E-14	6.62	0.04	7.0	5.2	8.8	0.9	0.4	2.3
37	2005-330/22:05:55	1511735696	2.39E-14	8.97	-0.06	7.3	5.4	9.2	0.7	0.3	1.8
38	**2005-358/14:37:41**	1514128018	6.68E-14	6.2	-0.03	6.8	5.0	8.6	0.9	0.4	2.3
39	**2005-358/14:49:12**	1514128709	4.32E-13	6.13	-0.03	6.8	5.0	8.5	1.2	0.5	3.1
40	**2005-358/15:57:10**	1514132787	2.07E-14	5.71	-0.02	6.4	4.7	8.1	0.8	0.3	2.1
41	2005-358/15:57:39	1514132816	4.30E-14	5.7	-0.02	6.4	4.7	8.1	0.9	0.4	2.4
42	2005-358/16:09:40	1514133537	7.77E-15	5.63	-0.02	6.3	4.7	8.0	0.7	0.3	1.8
43	2005-359/03:01:39	1514172656	6.11E-13	5.78	0.04	6.5	4.8	8.2	1.3	0.5	3.5
44	2005-359/04:06:40	1514176557	2.87E-14	6.19	0.04	6.8	5.0	8.6	0.8	0.3	2.1
45	**2005-359/04:06:52**	1514176569	9.60E-14	6.19	0.04	6.8	5.0	8.6	0.9	0.4	2.5
46	**2005-359/05:10:40**	1514180397	5.38E-14	6.62	0.04	7.0	5.2	8.8	0.8	0.3	2.2
47	2005-359/05:20:58	1514181015	4.33E-14	6.69	0.05	7.0	5.2	8.9	0.8	0.3	2.1
48	**2005-359/06:01:55**	1514183472	2.19E-14	6.98	0.05	7.1	5.3	9.0	0.7	0.3	1.9
49	**2005-359/06:26:12**	1514184929	7.14E-14	7.15	0.05	7.2	5.3	9.0	0.8	0.3	2.2
50	**2005-359/06:32:15**	1514185292	1.35E-13	7.19	0.05	7.2	5.3	9.0	0.9	0.4	2.4
51	**2006-016/08:08:18**	1516091868	5.75E-14	12.91	-0.08	6.5	4.8	8.2	0.9	0.4	2.4
52	**2006-056/05:15:38**	1519537530	1.26E-14	6.46	-0.03	5.4	4.0	6.8	0.9	0.4	2.4
53	**2006-056/17:46:16**	1519582569	1.65E-14	6.82	0.04	5.7	4.2	7.2	0.9	0.4	2.3
54	**2006-056/18:48:22**	1519586295	9.86E-15	7.15	0.04	6.0	4.4	7.5	0.8	0.3	2
55	2006-056/22:14:58	1519598691	1.32E-14	8.4	0.05	6.5	4.8	8.1	0.7	0.3	1.9
56	**2006-057/02:02:07**	1519612320	6.24E-14	9.88	0.07	6.6	4.9	8.4	0.9	0.4	2.4
57	**2006-057/02:05:38**	1519612531	3.55E-14	9.9	0.07	6.6	4.9	8.4	0.8	0.3	2.2
58	**2006-080/15:29:58**	1521648004	1.64E-14	11.6	0.08	6.7	4.9	8.4	0.7	0.3	1.9
59	2006-080/19:20:46	1521661852	1.79E-14	13.1	0.09	6.5	4.8	8.2	0.8	0.3	2
60	**2006-337/00:41:01**	1543799608	8.17E-14	4.99	0.04	12.6	9.3	15.8	0.4	0.2	1.1
61	**2006-337/00:46:46**	1543799953	4.60E-13	5.01	0.11	12.5*	9.3	15.8	0.5	0.2	1.4
62	**2006-337/00:55:19**	1543800466	4.77E-14	5.04	0.21	1.7	1.3	2.1	0.4	0.2	1.1
63	**2006-337/00:59:05**	1543800692	1.55E-14	5.05	0.25	12.5	9.2	15.8	0.3	0.1	0.9
64	**2006-337/01:18:39**	1543801866	1.86E-14	5.13	0.48	12.4	9.2	15.6	0.4	0.1	0.9
65	**2006-337/01:26:38**	1543802345	3.85E-14	5.16	0.57	12.4*	9.1	15.6	0.4	0.2	1
66	**2006-337/04:59:37**	1543815124	1.57E-13	6.24	2.93	10.6*	7.8	13.3	0.6	0.2	1.5
67	2006-337/05:49:38	1543818125	1.75E-14	6.54	3.43	10.1	7.5	12.8	0.4	0.2	1.2
68	**2006-349/04:52:09**	1544851483	4.86E-14	7.89	-2.66	8.9	6.5	11.2	0.6	0.2	1.6
69	**2006-349/16:06:48**	1544891962	3.95E-14	10.08	2.6	8.3	6.1	10.5	0.6	0.3	1.7
70	**2007-130/19:21:23**	1557518117	8.31E-14	4.8	0.08	10.3*	7.6	13.0	0.5	0.2	1.5
71	**2007-130/19:32:19**	1557518773	5.98E-13	4.75	-0.02	10.3*	7.6	13.0	0.7	0.3	1.9
72	**2007-130/19:37:15**	1557519069	4.10E-14	4.73	-0.06	10.3	7.6	13.0	0.5	0.2	1.3
73	**2007-130/19:44:45**	1557519519	6.15E-14	4.7	-0.13	10.3	7.6	13.0	0.5	0.2	1.4
74	**2007-130/19:50:29**	1557519863	3.34E-14	4.68	-0.18	10.3	7.6	13.0	0.5	0.2	1.3
75	**2007-130/19:51:50**	1557519944	1.49E-13	4.67	-0.2	10.3	7.6	13.0	0.6	0.2	1.6
76	**2007-130/19:53:50**	1557520064	3.66E-14	4.66	-0.21	10.3*	7.6	12.9	0.5	0.2	1.3
77	**2008-130/23:08:03**	1589067930	1.16E-13	4.67	0.76	14.3*	10.6	18.0	0.4	0.2	1
78	**2008-130/23:57:13**	1589070880	2.02E-14	4.5	0.1	14.6*	10.8	18.5	0.3	0.1	0.8
79	**2008-131/00:20:35**	1589072282	4.29E-14	4.44	-0.21	14.7*	10.9	18.6	0.3	0.1	0.9
80	**2008-131/02:18:04**	1589079331	5.10E-14	4.3	-1.75	14.1*	10.4	17.8	0.3	0.1	0.9
81	**2008-131/03:00:00**	1589081847	8.66E-14	4.32	-2.26	13.5	10.0	17.0	0.4	0.2	1
82	**2008-131/03:16:31**	1589082838	1.34E-13	4.35	-2.46	13.2	9.8	16.7	0.4	0.2	1.1
83	**2008-131/03:19:14**	1589083001	6.43E-14	4.35	-2.49	13.2*	9.7	16.6	0.4	0.2	1

The columns of the table show the number of the spectrum (#, in order of detection); the time of detection in coordinated universal time (UTC) and as measured by the spacecraft clock (SCLK); the amplitude of charge measured at the CDA ion grid (QI (C)); the spacecraft's distance to Saturn's rotation axis ($R(R_S)$; where R_S = 60,268 km is Saturn's radius); the spacecraft's distance to the ring plane ($Z(R_S)$); grain impact speeds (in kilometres per second, see below); and the corresponding grain radii estimates (in micrometres). For the grain impact speeds, the velocity V_{imp} is derived assuming that grains are in circular Keplerian orbits, and $V_{-\sigma}$ and $V_{+\sigma}$ are the $\pm 1\sigma$ of the grain impact speed distributions, inferred from an E-ring model derived from numerical simulations[73,74].
The grain radii shown in the last three columns are calculated on the basis of V_{imp}, $V_{-\sigma}$ and $V_{+\sigma}$ using equation (3.37) of ref. [78].
Events for which the UTC time is shown in bold fonts are the 64 high-quality spectra (see Methods, 'Selection of 64 high-quality spectra for Fig. 1 and Extended Data Figs. 1 and 3'). Speeds marked with an asterisk denote spectra in which one or more hydrogen cations (H^+, H_2^+, H_3^+) are present, which is used as an independent and reliable criterion for impact speeds larger than 10 km s^{-1} even if the number derived from the assumption of circular orbits (V_{imp}) is lower.